Temperature profiles combined from lidar and airglow measurements

Thomas Trickl[1], Hannes Vogelmann[1], Michael Bittner[2,5], Gerald Nedoluha[3], Carsten Schmidt[2], Wolfgang Steinbrecht[4] and Sabine Wüst[2]

[1]Karlsruher Institut für Technologie, Institut für Meteorologie und Klimaforschung (IMK-IFU), Kreuzeckbahnstr. 19, 82467 Garmisch-Partenkirchen, Germany

[2]Deutsches Zentrum für Luft und Raumfahrt (DLR), Deutsches Fernerkundungsdatenzentrum (DFD), 82234 Oberpfaffenhofen, Germany

[3]Naval Research Laboratory, 4555 Overlook Avenue, SW, Washington, D.C. 20375, U.S.A.

[4]Deutscher Wetterdienst, Meteorologisches Observatorium Hohenpeißenberg, Albin-Schwaiger-Weg 10, 82383 Hohenpeißenberg, Germany

[5] Universität Augsburg, Institut für Physik, 86159 Augsburg, Germany

Correspondence to: Dr. Thomas Trickl, thomas@trickl.de, Thomas-Knorr-Str. 47, D-82467 Garmisch-Partenkirchen, Germany; tel. +49-8821-50283; Dr. Hannes Vogelmann, hannes.vogelmann@kit.edu, Karlsruher Institut für Technologie, IMK-IFU, Kreuzeckbahnstr. 19, D-82467 Garmisch-Partenkirchen, Germany; tel.: +49-8821-258

Abstract. In this study we examine the performance of the 354.8-nm Rayleigh temperature channel of the Raman lidar at the Schneefernerhaus high-altitude research station (UFS) in the Bavarian Alps (at 2675 m a.s.l.). The temperature reference value of the retrieval is adjusted to match the temperature determined from the OH* airglow around 86 km by the GRIPS instruments at UFS. In this way the quality of the 1-h measurements of the lidar is improved above 70 km. Comparisons were made between the UFS lidar, the MLS (Microwave Limb Sounder) satellite-borne instrument and the 354.8-nm temperature channel of Hohenpeißenberg (MOHp) differential-absorption ozone lidar. Between 35 km and 70 km we see a positive offset of the UFS temperatures with respect to the MLS values of up to about 9 K. This behaviour just slightly exceeds the expectations from earlier work. Despite a horizontal distance of just 40 km between UFS and MOHp acceptable agreement below 70 km was found in several cases. However, in general, the MOHp temperatures were slightly lower than those above UFS. We discuss potential technical issues and suggest solutions for upgrading the UFS lidar system. A significant enhancement of the laser repetition rate is recommended.

Key words: Temperature, stratosphere, mesopause, lidar, MLS, OH, airglow

1. Introduction

Accurate temperature measurements at short time intervals up to the mesosphere are an important contribution to climate research and for a better understanding of the atmospheric energy balance, in particular with respect to gravity waves. This can yield information for improving atmospheric and climate models that usually only consider the comparatively small-scale gravity waves in the form of parameterizations (e.g. Kim et al., 2003; Medvedev et al., 2019). These are simplified mathematical formulations of the wave effects, as exact calculations are hardly possible for resource reasons.

In the lower atmosphere the vertical distribution of the temperature is mostly obtained from the routine radiosonde ascents that are typically carried out up to roughly 30 km twice per day. Routine measurements up to higher altitudes are to a major extent provided by satellite-based sensors yielding temperature profiles up to more

than 90 km (e.g., Curtis et al., 1974; Russell et al., 1999; Waters et al., 2006;). These measurements are carried out with a rather dense global coverage.

These observations are complemented by ground-based lidar measurements. Leblanc et al. (1998) stated that lidar measurements provide the best vertical resolution and accuracy for middle-atmosphere temperature studies. The most commonly applied lidar method is based on Rayleigh scattering (e.g., Hauchecorne and Chanin, 1980; Hauchecorne et al., 1991; Fishbein et al., 1996; von Zahn et al., 2000; Keckhut, 2004) and yields temperatures typically in the mostly aerosol-free range between 30 and 85 to 95 km. The temperature inversion from Rayleigh backscatter profiles is the key approach within the global Network for the Detection of Atmospheric Composition Change (NDACC, https://ndacc.larc.nasa.gov). Also, daytime measurements, based on extremely narrowband spectral filtering and a very small field of view, have been demonstrated (e.g., Gille et al., 1991; von Zahn et al., 2000).

The measurements times can be excessive and must be reduced to capture the short-term temperature variability. This is achieved by the use of a powerful laser and a large receiver. Sica et al. (1995) have used a 2.65-m-diameter spinning liquid-mercury mirror in order to collect a maximum of 532-nm light backscattered from 12 W from a frequency-doubled Nd:YAG laser and, in this way, have achieved temperature measurements up to more than 100 km within 6 h of lidar operation and with vertical bin sizes of 48 m. At lower altitudes, shorter measurement times are possible. The propagation of tidal and gravity waves was visualized in the altitude range between 33 and 50 km (Sica, 1999).

Traditionally, backward retrievals starting at the highest useful altitude are applied (Hauchecorne and Chanin, 1980). This approach converges to the correct solution within roughly 15 km. In order to obtain more quantitative data also in the uppermost range forward retrievals based on optimum-estimation methods have been successfully applied (Khanna et al., 2012).

Above 80 km fluorescence lidar methods are used both for density and temperature measurements, up to 110 km. The sensitivity of laser-induced fluorescence methods is very high and has made possible single-atom detection in the laboratory (e.g., Ott, 2016). In the atmosphere its application is limited to low-density conditions where fluorescence quenching is avoided. Metallic species, in particular sodium, potassium and iron atoms, have been successfully detected and used for temperature retrievals (e.g., Bowman et al., 1969; Blamont et al., 1972; Mégie et al., 1978; Fricke and von Zahn, 1985; Granier et al., 1989; She et al., 1990; Papen et al., 1995; Arnold and She, 2003; Xu et al., 2006). This method has allowed for daytime operation (e.g., Chen et al., 1996; Chu et al., 2001; Höffner and Lautenbach, 2009)

A combination of all the three lidar methods (rotational Raman scattering (e.g., Arshinov et al., 1983; Behrendt, 2005; Serikov and Bobrinikov, 2009), fluorescence, and Rayleigh scattering) has been applied to generate a composite temperature profile from 1 km to 105 km (Alpers et al., 2004). This approach has been extended to daytime operation by narrowband spectral filtering (Gerding et al., 2010; Kopp et al., 2015; see also von Zahn et al., 2000). The propagation of waves could be studied in an enormous range between 35 km and 104 km.

Alternatively, temperature information has been obtained from ground-based measurements of the OH* airglow (e.g., Sivjee, 1992; Scheer et al., 1994; Bittner et al., 2000; 2002; Beig et al., 2003; Reisin et al., 2014; Wüst et al, 2023). This method is not height resolved, but benefits from the rather confined range of the OH* airglow with its peak emission height between 85 and 87 km and a full width at half maximum (FWHM) between 6 and 9 km on average for the Alpine region (Wüst et al., 2017). Peak emission height and FWHM show an annual and a semi-annual variation due to vertical transport processes at this height. Latitudinal and longitudinal variations exist to a small extent (Wüst et al., 2020). Those values are retrieved from multi-year satellite data. From

ground-based OH* airglow measurements some height information can be deduced based on the altitude-dependence of the vibrational population (e.g., Lopez-Moreno et al., 1987; von Savigny et al., 2012; Schmidt et al., 2018, Noll et al., 2023)) or from the relation between the column-integrated volume emission rate and peak emission height (e.g., Liu and Shepherd, 2006; Mulligan et al., 1995). The second method is based on the functional relationship between both parameters; this must first be determined, e.g., by adding height-resolved satellite measurements. In addition, the OH* layer has frequently been observed in limb geometry by rocket- and satellite-borne spectrometers or radiometers (e.g., Baker and Stair, 1988; Takahashi et al., 1996; Englert et al., 2010; von Savigny et al., 2013; Noll et al., 2017; Wüst et al., 2017; Li et al, 2021). Von Zahn et al. (1987), She and Lowe (1998) and Schmidt et al. (2018) compared temperature measurements of sodium lidar systems with results from OH* spectrometers. It should be noted that ground-state ($v'' = 0$) OH molecules have been observed by laser-induced ultraviolet fluorescence, i.e. in the A $^2E^+$ - X ^{2}II(0, 0) band at heights between 75-85 km (Brinksma et al., 1998). The chemiluminescent OH*-layer addressed by passive remote sensing instruments consists of pure rotational-vibrational transitions ($v'' \leq 9$) within the X ^{2}II electronic state and, originating from a different chemical reservoir, and peaks at higher altitudes (see Baker and Stair, 1988; Wüst et al., 2017).

In 2018 measurements of the atmospheric temperature in the stratosphere and the mesosphere were started with the 355-nm channel of the big Raman-Rayleigh lidar system at the Schneefernerhaus Alpine high-altitude station (UFS, 2675 m a.s.l.) in the Bavarian Alps (Klanner et al., 2021). These activities extend the water-vapour (Vogelmann and Trickl, 2008) and aerosol (Trickl et al., 2024) sounding at this site. The backscatter profiles, acquired within one hour, currently cover a range up to roughly 90 km. The inversion of these profiles yields temperature data up to more than 80 km if a reliable upper-end temperature reference is available. At UFS we benefit from using the temperature data from the OH* measurements at the station as a reference. This is a clear advantage with respect to comparisons with satellite data, obtained on somewhat remote orbits, or with models of unknown reliability (see Klanner et al., 2021).

In this paper, we aim at validating this new instrument, a task mandatory because of the features of the large detection system and in view of the planned archiving in the data base of the Network for the Detection of Atmospheric Composition Change (NDACC, https://www.ndacc.org). We look for the principal performance and, thus, just give comparisons with a limited number of instruments carefully characterized elsewhere (for references see below). In particular, we judge the performance by nearby lidar measurements and derive recommendations for improvements and further tests.

2. Data sources

2.1 Rayleigh backscatter measurements at 354.8 nm with a large lidar system at the Schneefernerhaus high-altitude station (Zugspitze, Germany)

Since 2009 a high-power Raman lidar system has been developed by a team from the Institute for Atmospheric Environmental Research (Garmisch-Partenkirchen, Germany; since 2009 Karlsruher Institute of Technology, IMK-IFU) that yields profiles of the water-vapour mixing ratio up to more than 20 km within one hour (Klanner et al., 2021). This lidar is located at the high-altitude station Schneefernerhaus (Umweltforschungsstation Schneefernerhaus, UFS, 47° 25′ 00″ N, 10° 58′ 46″ E, 2675 m a.s.l.) on the south side of Mt. Zugspitze (2962 m a.s.l.), about 9 km to the south-west of IMK-IFU. Because of its elevation UFS provides mostly free-tropospheric conditions (Carnuth et al., 2002). As pointed out by Trickl et al. (2024) the high base elevation yields a significant gain in backscatter signal even in the stratosphere. The system is operated side by side with a differential-absorption water-vapour lidar (DIAL; Vogelmann and Trickl, 2008; Trickl et al., 2014; 2015; 2016)

which allows for optimum calibration, also considering an absence of a significant bias, at least within the first kilometres (Vogelmann et al., 2011; Trickl et al., 2016).

The Raman lidar system benefits from a large Newtonian receiver with 1.5 m diameter and a XeCl laser with up to 180 W emission in single-line operation at a repetition rate of 350 Hz (Coherent, Lambda SX, with an extended cavity containing an intracavity etalon and a polarizer).

This system can additionally yield temperature measurements by two methods. Up to the lower stratosphere the temperature may be retrieved from two rotational Raman channels. This approach has been successfully tested (Höveler, 2015), but has not yet entered routine operation because the focus has so far been on optimizing the performance of the H_2O channel.

The second approach is inverting one of the two Rayleigh backscatter profiles of the lidar at 307.96 nm and 353.14 nm. The emission for the preferred second channel was first generated by stimulated Raman shifting the output of the XeCl laser in hydrogen (Klanner, 2022). However, the performance at 353.14 nm was not reliable at the high repetition rate of 300 Hz. As a consequence we added a frequency-tripled injection-seeded Nd:YAG laser (Continuum, Powerlite Precision 8020) previously used in our water-vapour DIAL. This laser emits at the wavelength of 354.81233 nm and yields pulse energies of 170 mJ, substantially more than the emission planned from the Raman-shifted excimer laser. However, the repetition rate is limited to 20 Hz. The choice of the ultraviolet wavelength provides the advantages of a larger backscatter signal than for 532.2 nm. Most importantly, the light-absorption by ozone at 532.2 nm is avoided (Trickl et al., 2024).

A general design feature in our lidar systems is the absence of optical fibres. In this way, coupling losses, near-field issues and fluorescence effects are avoided. In addition, the polarization of the transmitted radiation is conserved which is essential for the chosen optical configuration of the detection polychromator (Fig. 8 of Klanner et al., 2021). The 354.8-nm channel is spectrally filtered by a combination of a filter (Semrock), transmitting 85 % – 90 % of the radiation between 330 and 355 nm and blocking spectral contributions outside this range by at least 10^5, and a narrowband filter with a width of less than 1.2 nm (Alluxa).

A key issue for temperature measurements is a high quality of the detection electronics: An uncertainty of (e.g.) the order of 1 K means a relative uncertainty of the measurements of less than 0.5 %. Here, we benefit from the experience gained from our older systems (e.g., Trickl et al., 2020; 2023; 2024). The backscattered radiation is detected with Hamamatsu R7400U-03 photomultiplier tubes (PMTs) with actively stabilized sockets from Romanski sensors (RSV). In the following we describe, for simplicity, the signal voltages as positive values instead of the negative ones emerging from the detectors. The performance of these detectors is highly linear for peak analogues signals cautiously set to 70 mV (for 50 Ω termination) and less (Trickl et al., 2020; 2024). Here, this is achieved by adjusting the laser pointing in order to maintain the maximum far-field signal level. However, the analogue output is ten times more sensitive to the background signal than the PMTs from the older 5400 series (Trickl et al., 2020). Undershooting occurs at analogue background levels exceeding 1 mV ~~(for 50 Ω termination)~~, which does not matter during night-time. However, also excessive lidar backscatter could, in principle, lead to some undershooting and we have, therefore, limited the peak analogue signal even to less than the 70 mV ~~(into 50 Ω)~~ successfully applied by Trickl et al. (2020).

The output is registered in 12-bit transient digitizers at a range-bin size of 7.5 m (Licel). This model was modified in 2010 for our ozone DIAL with a ground-free input, which was also implemented in all systems digitizer systems purchased in the following. The Licel transient digitizer is optimized for very low noise (less than $\pm 10^{-5}$ of the measurement range for 4096 laser shots), but, in contrast to the previously used system from DSP Technology (model DSP 2020; Trickl et al., 2020), features a slight exponential wing that grows with the

area of the lidar backscatter signal. This wing could be easily corrected in the case of the ozone DIAL because of the short decay time of the signal (Trickl et al., 2020), but is difficult to quantify for the long signal at longer wavelengths. An exponential curve is subtracted, derived from a comparison with the photon-counting results at high altitudes (see below). The decay constant is the same for all retrievals. An example is given in Fig. 1 (for more details see Sect. 3.1).

Parallel to this detection channel for the analogue signal we count the individual photons in a MCS6a multichannel scaler (FAST ComTec) with a pulse-pair resolution of 0.2 ns, more than sufficient for the 1.5-ns-wide pulses from the detector. Because of the near-field overload of the sequential data transfer to the computer we delay the start of the counting system by 10 µs. The perfect linearity of the photon-counting channels has been verified by the validation of our water-vapour measurements (Klanner et al., 2021) and the performance of our stratospheric aerosol measurements (Trickl et al., 2024), at least to up to 45 km. We have been optimistic that the perfect linearity extends to much higher altitudes since the settling time of artefacts for this type of PMT seems to be rather short. For the threshold voltage of −4 mV set at the fast discriminator (RSV) testing with closed detector entrance revealed that the detection is free of "dark counts". For the temperature measurements, the night-time background count rate is of the order of 0.2 counts per 7.5-ns bin and hour at the maximum distance of 120 km, which allows for keeping the far-field signal-to-noise ratio as high as possible.

2.2 Microwave Limb Sounder on board the Aura satellite

The Microwave Limb Sounder (MLS; Waters et al., 2006) on board the Aura satellite (Schoeberl et al., 2006) was launched to space in 2003. The instrument not only detects thermal emission from various molecules (most recently, e.g., Nedoluha et al., 2024; 2025), but also yields vertical profiles of the atmospheric temperature up to almost 100 km. 3500 vertical profiles are produced per day. The temperature retrieval is based on limb radiances near the oxygen spectral lines at 118 GHz and 234 GHz. The limb-tangent pressure is derived from the shape of the broadened O_2 lines.

Schwartz et al. (2008) analysed the quality of the temperature and geopotential height determined from the measurements. Comparisons with other satellite-borne instruments indicate a negative temperature bias for altitudes corresponding to pressures of 1 mbar and less. Mevedewa et al. (2014) report a negative bias of about −10 K of the MLS temperature with respect to that obtained from OH measurements above 80 km.

For the examples shown in this paper there are just two of the 14 cases with a passage almost perfectly above Garmisch-Partenkirchen during the night-time lidar observations. Given the enhanced wave activity that can be expected above the Alps (e.g., Hannawald et al., 2019) this limits the quality of comparisons.

The geopotential height is converted to absolute height for the comparisons.

2.3 GRIPS OH* chemiluminescence

A closer spatial agreement with the UFS lidar is achieved with the routine OH* airglow measurements at UFS in the mesopause region. The OH spectra are registered with the Ground-based Infrared P-branch Spectrometer (GRIPS) instrument (Schmidt et al., 2013), integrated in the global Network for the Detection of Mesosphere Change (NDMC; https://ndmc.dlr.de; e.g., Reisin et al., 2014). The centroid altitude of the airglow is 86 ± 2 km and slightly varies with the season (von Zahn et al., 1987; Baker and Stair, 1988; She and Lowe, 1998; Wüst et al., 2017, 2020). The aims of the research are an identification and quantification of the influence of climate change, the detection of solar activity effects, the influence of atmospheric dynamics (wave activity) and the validation of satellite instruments.

A survey on the relevant spectroscopic data and literature is given, e.g., by Noll et al. (2020) and Wüst et al. (2023). Wüst et al. (2023) provide a review on the recent achievements of OH* measurements. Only transitions emerging from low-lying vibrational levels appear to be suitable for sufficiently quantitative temperature derivations and we, therefore, use the low-lying (3,1) OH* transitions (Bittner et al., 2002; Noll et al., 2017). The lack of vertical resolution and the relatively large thickness of the OH* layer yields temperatures that are weighted means over a layer of the atmosphere extending over roughly 8 km.

The GRIPS instrument at UFS is oriented for slant-path detection which means that the OH* layer is reached approximately above Bozen (46.6° N, 11.0° E, Italy) south of the Central Alps, at a horizontal distance of roughly 90 km. The night-time temperature time series exhibit variations such as can be seen in the three examples shown in Fig. 1. The amplitudes of the T variations can be as high as 10 K, rarely more. In order to gain insight into the horizontal extent of these structures we, therefore, compared the GRIPS measurements with those at Oberpfaffenhofen (OPN, 48.1°N, 11.3°E, about 77 km to the north) during the same nights. The full-night average temperatures at both sites mostly agree within 1 to 3 K. The structures measured from the OPN station are not identical, but at least similar (see right panels in Fig. ~~1~~2). The cases with pronounced differences demonstrate that temperature changes can occur on a confined spatial scale. This leads to uncertainties for the comparisons in Sect. 3.

The temperature in the OH* layer exhibits a pronounced seasonal dependence varying between about 170 K in summer and 220 K in winter, with average amplitudes of 17.5 K and 3.0 K of the annual and semi-annual component (see Schmidt et al., 2023). There is no consistent trend in the night-time series used this study, but a general tendency for a slight rise. Systematic temperature changes throughout the night caused by the semidiurnal migrating (12 h) tide, maximising in winter can be expected. On average this can lead to a 4-5 K temperature increase from 21 CET to 3 CET at UFS in January (compare Fig. 7 in Schmidt et al (2023)). As far as the nights used in this study show variability at all, it appears to be dominated by shorter period structures, which in some cases exhibit substantial amplitudes (~~compare~~ Figure 2).

2.4 Temperature measurements with the Hohenpeißenberg ozone DIAL

A considerable chance for the validation of the UFS lidar is given by the routine night-time temperature measurements with the ozone differential-absorption lidar (DIAL) at the Meteorological Observatory Hohen-peißenberg (MOHp) of the German Weather Service. This station is located just 42 km to the north of UFS.

The MOHp DIAL is technically similar to the UFS lidar (Wing et al., 2021) which is an excellent basis for comparisons. For the T measurements it is also operated at 354.8 nm using a frequency-tripled Nd:YAG system (Innolas, model SpitLight 600, 120 mJ per pulse, 20 Hz repetition rate). The PMT type is similar (Hamamatsu, R9880U-110, with home-made socket) and was compared with the PMT type used at UFS without showing a difference in lidar backscatter profile. The diameter of the principal mirror of the Newtonian telescope is smaller (1.0 m), but the data acquisition is extended to full nights, which results in a high signal-to noise ratio. Exclusively photon counting is applied (FAST, P7882-2, maximum count rate 200 MHz).

The data are averaged over 150 m and, after the evaluation, smoothed to 450 m. The temperatures are routinely stored in the NDACC data base (https://ww-air.larc.nasa.gov/missions/ndacc/data.html#) from 27 km to roughly 95 km.

3. Inversion of the UFS lidar data

3.1 Temperature retrieval

The temperature profiles are retrieved from the 354.8-nm backscatter profiles as described by Klanner et al. (2021). Here, we give a few more details than in the preceding publication, based on the experience gained from the more recent measurements.

The algorithm is a modified version of the downward inversion method introduced by Hauchecorne and Chanin (1980; see also Shibata et al., 1986). This method has the advantage of self-correction within roughly 15 km from the top (reference) altitude and is less complicated than the forward inversion proposed by Khanna et al. (2012) which might be implemented at a later stage. However, we benefit from the OH* airglow measurements at UFS that allow us to shift the reference temperature to a value that yields a good match of the T profile with the OH temperature at 86 km, the average altitude of the OH* layer (Wüst et al., 2017). In cases in which the reference altitude has to be chosen below 86 km an extrapolation is estimated. In cases in which the reference altitude is above 86 km we used the temperature from the U.S. Standard Atmosphere (1976) in a first step and apply a correction in a following retrieval that shifts the temperature at 86 km to a value within the uncertainty range of the GRIPS temperature.

The main source of data is the photon-counting signal. We select a bin size of 51.2 ns, which represents a length of 7.6747 m. The PMTs were tested without input radiation and turned out to be free of background counts for 1 h of data accumulation in a single bin. Thus, no cooling of the detector is required. As mentioned, in night-time atmospheric measurements the average background count rate has been as low as roughly 0.2 counts bin^{-1} h^{-1} (Fig. 1). This is the result of careful spatial filtering and the narrow spectral filtering. This performance to a major extent excludes artefacts such as those described by Wing et al. (2018a). The backscatter profiles from the counting system are interpolated to match the 7.4948 m bin size and the vertical grid of the transient digitizer.

We start the data evaluation with visualizing the raw data and their conversion. In Fig. 1 we show an example of backscatter profiles from 9 October 2021. After determining the zero point of the distance scale we average the content of two neighbouring bins and double the size of a single data bin to 14.9896 m, which reduces the number of bins to 8000 (119.917 km). The analogue data are substantially noisier than the photon-counting data and exhibit a background drift tentatively ascribed to the performance of the transient digitizer. The 355-nm analogue profile was corrected by subtracting 3.22×10^{-4} $\exp(-8.0\times10^{-6}\times r)$, with r being the distance above the lidar in metres. The constant of the exponential decay was used in all measurements evaluated since April 2021. This decay is 7 times slower in comparison with that in our ozone DIAL (Trickl et al., 2020) and is observable just because of the excessive operating range and the longer averaging. The fast decay component of the DIAL (277 to 313 nm) cannot be resolved because of the slower decay of the 355-nm signal, also implying the absence of absorption in ozone.

The analogue data are used from about 10 km to 30 km. As can be seen in Fig. 1 the correction is crucial for obtaining optimum temperature profiles from the analogue data for distances r up to 30 km. The data correction must be made with care because of the enormous requirements for the temperature measurements. Below 10 km the signal is partially cut off by one side (blade) of the entrance aperture, the laser beam being adjusted to limit the near-field peak signal. Above 30 km the photon-counting signal is taken where it is fully linear. No dead-time correction has been implemented in this channel as frequently done in lidar systems based on counting alone. All backscatter signals are carefully compared with simulations from meteorological data (see also below).

The analogue measurement in Fig. 1 is the best in comparison with those in the other measurements obtained since spring 2021. In other cases, slight deviations from the clean exponential behaviour were observed that we

tend to ascribe to interference of the magnetic field of the laser flashlamps as found in earlier work (e.g., Trickl , 2010). The use of a diode-laser-pumped laser system is planned (see Sect. 4). For such a laser system we have not found any similar interference (Trickl et al., 2024).

For reducing the data noise we apply altitude-depended smoothing with a numerical filter as described by Trickl et al. (2020). The bin interval of the Blackman-type filter is nonlinearly enhanced using the formula

$$a + i^2 \times b$$

at bin i (size 14.9896 m), with normally a = 20 and b = 4×10^{-5}. This results in a variation of the VDI (1999) vertical resolution from 58 m at the ground to 1216 m at 50 km and a maximum of 2908 m at and above 76.7 km a.s.l. (Trickl et al., 2020; VDI, 1999; see (Iarlori et al., 2015; Leblanc et al., 2016) for other definitions). The VDI resolution is defined as the range difference between 25 % and 75 % of the response to a Heaviside step. Above this, the vertical resolution stays constant to limit the computation requirement.

As described by Klanner et al. (2021) we first calculate the atmospheric density in a fully quantitative Klett-type approach with downward integration from the far end (Klett, 1981; 1985):

$$n(r) = \frac{n(r_{ref})\ r_{ref}^2 \mathrm{S}(r_{ref})}{r^2 \mathrm{S}(r) + 2n(r_{ref})\sigma_R \left[\int_r^{r_{ref}} r'^2 \mathrm{S}(r') dr' \right]} , \quad (1)$$

S*(r)* being the backscatter signal, r_{ref} the reference distance and σ_R the Rayleigh extinction coefficient. Here, the misprint in Eq. 1 of Klanner et al. (2021) is corrected that has not been part of the computer program. The far-end reference density $n(r_{ref})$ is varied for matching the density derived from the Munich radiosonde (launched at Oberschleißheim, station 10868, about 100 km roughly to the north), also making comparisons with the densities from NCEP (National Centers for Environment Prediction) at higher altitudes. We download the sonde data from https://weather.uwyo.edu/ upperair/sounding.html. The NCEP altitudes, pressures and temperatures are taken from the web site of the Network for the Detection of Atmospheric Composition change as calculated for Garmisch-Partenkirchen (https://www-air.larc.nasa.gov/ missions/ndacc/data.html?NCEP=ncep-list). The NCEP listings are available up to roughly 55 km.

From the density *n* we obtain the temperature profile by applying

$$\mathrm{T}(z) = \mathrm{T}(z_0)\frac{n(z_0)}{n(z)} + \frac{m_{air}}{k\ n(z)} \int_z^{z_0} n(z')g(z')dz' , \quad (2)$$

with *z* being the altitude above sea level, z_0 the far-end reference altitude, m_{air} = 28.9644 u (U.S. Standard Atmosphere, 1976; 1 u = 1.66053904×10^{-27} kg (Mohr et al., 2016)) the mass of an "average air molecule", and g the gravitational acceleration,

$$g(z) = g_0 \left(\frac{r_E}{r_E + z}\right)^2 ,$$

with g_0 = 9.80665 m s^{-1} and the earth radius r_E = 6356766 m (U.S. Standard Atmosphere, 1976). In the U.S. Standard Atmosphere the atmosphere is regarded as well mixed up to 86 km, which suggests to be cautious at the highest altitudes accessible.

The inversion starts at the highest reasonable altitude, mostly below the upper end of the density profile. Normally, we take the temperature for the start altitude from the U.S. Standard Atmosphere (1976) as the reference. The algorithm in Eq. 2 is self-correcting: Within 15 km of downward integration the temperature is

does no longer vary as a function of the reference value by more than ±2 K (Klanner et al., 2021), as a consequence of the density dependence of the first term of Eq. 2. It turned out that the influence of the reference density (Eq. 1) is very low and can be neglected for the careful adjustment made (see above).

In eight of the fourteen cases examined we had to make adjustments of the reference temperatures to match the temperature of the GRIPS instrument at 86 km, or, in one case without GRIPS measurements, the range of MLS values. For a perfect comparison of lidar and GRIPS an extension of the operating range of the lidar to more than 100 km is desirable. Wing et al. (2018a) recommended to use the MSIS model output as a reference. The result was not satisfactory at all (Klanner et al., 2021) and we decided to use the GRIPS temperatures.

The retrieval of temperature from lidar data is a highly demanding task. For instance, an uncertainty of 1 K means a relative uncertainty of 0.33 % at a temperature of 300 K. Thus, a very high quality of the backscatter signals is a prerequisite for reasonable results.

Aerosol corrections have been tested and lift the temperature in a range around 22 km, typically by 2 to 4 K under the conditions of the cases chosen. The aerosol backscatter coefficients are taken from the stratospheric aerosol measurements (Trickl et al., 2024) from adjacent days and converted from 532.24 nm to 354.8 nm by multiplication with 1.992 (Jäger and Deshler, 2002; 2003). However, such an effort makes sense just if the quality of the exponentially corrected analogue signal matches that in Fig. 1 which was the case just for two measurements (16 November 2018 and 9 October 2021). In the other cases, the analogue signal background exhibited slight modulations perhaps caused by the magnetic field of the flashlamp-pumped laser. Here, the exponential correction is adjusted to generate temperature values matching those from the midnight Munich radiosonde (station 10868).

3.2 Uncertainties

As pointed out in the U.S. Standard Atmosphere (1976) the atmospheric composition is homogeneous mixed up to 86 km. Local short-term perturbations are averaged away by the long signal acquisition time of 1 h.

The uncertainty from shot noise, as derived from the smoothed signal, is of the order of 10 K at 70 km. We use a scaling law

$$u = \sqrt{u_0^2 + (u_1 \frac{r^2}{r_{ref}^2})^2 + (u_2 S(r))^2}\ , \qquad (3)$$

for the uncertainties, with coefficients u_0, u_1, and u_2 that are estimated by comparison with reference measurements at lower altitudes and the shot noise at higher altitude. The second term in Eq. 3, quadratic in r, reflects the quadratic rise of the noise of the unsmoothed quantities. We select the reference distance r_{ref} at the upper end of the data evaluation range. By the approach with Eq. 3 considerable computation efforts have been avoided. The results of ~~the night-time series (~~Sect. 4~~.4)~~ verify the approximation.

4. Results

4.1 UFS lidar results

The lidar test phase presented in Sects. 4.1 to 4.3 covers the 14 measurements made between November 2018 and February 2022. In addition, four separate night-time series are presented in Sect. 4.4.

In Fig. 3 we show the result of a revised data evaluation of the example shown by Klanner et al. (2021) based on the slightly enhanced smoothing described in Sect. 3.1 and an exponential correction of the analogue profile that was missing in the earlier evaluation. In addition, an aerosol correction was made that resulted in good agreement with the temperature profile of the Munich radiosonde down to 12 km. The ripple below 32 km is a result of the aerosol correction. Below 12 km the signal was partly cut off by rotating the laser beam to shift the return bundle towards one side the entrance aperture of the detection system in order to limit the maximum signal.

The GRIPS value was determined from an average of the GRIPS temperatures during the measurement period of the lidar, which was done for all cases. The error bar represents the standard deviation for that period and does not include the uncertainty due to the missing co-location caused by the ~~shifted horizontal position of the~~slant-path OH* ~~layer~~ measurements ~~south of the Central Alps~~(see Sect. 2.3). This influences the results in an uncertainty of ±5 K, sometimes more. The GRIPS value in this example agreed sufficiently well with the lidar temperature generated by initiating the retrieval with the U.S. Standard temperature at 88 km. Thus, the calibration was not shifted.

The NCEP data agree well with the radiosonde temperatures up to the operating range of the balloon. There is a small deviation with respect to the lidar at 40 and 46 km. We do not know if this bias is caused by a vertical shift of the NCEP profile.

We also added temperature profiles from MLS and the MOHp lidar. Unfortunately, no T profile from MOHp was available for the same night, and we took the results from the two neighbouring measurement nights. The average of both MOHp profiles agrees quite well with the UFS profile to about 70 km. The MLS profiles are shown for about 13:31 CET (Central European Time, three thin orange lines) and about 3:05 CET on 17 November 2018 (three blue lines), named “noon” and “midnight”, respectively. The agreement should be better for the “midnight” measurement, but the best agreement is limited to the spike region around 64 km. In principle, this could be ascribed to the pronounced difference in longitude.

4.1 Comparisons of the temperatures from the UFS lidar and the NCEP archive

Up to the burst altitudes of the balloons (mostly 30 to 33 km) the temperature of the Munich radiosonde is nicely reproduced (see examples: Fig. 3 and Sects. 4.2, 4.3). For higher altitudes the temperatures are compared for all NDACC stations from the NCEP data. The NCEP profiles are listed up to roughly 55 km. Again, geopotential heights are converted to absolute heights.

Trickl et al. (2024) found for the evaluation of stratospheric aerosol that the Rayleigh reference profiles calculated from the NCEP density and temperature data look highly reliable up to the chosen Klett (1983) reference distance of 45 km (absolute altitude 47.675 km). However, the requirements for the temperature are much higher. For the temperature data we found, in comparison with the UFS lidar, reasonable agreement up to 35 km, but sometimes deviations above this altitude (and below 50 km) of up to about 10 K occur (see Fig. 3 and examples in the following sections; in one case even more). Sometimes there is the impression of a vertical shift of the NCEP profile or a slightly wrong gradient in the range of the strongest temperature increase. The NCEP profiles are calculated for noon UTC (13:00 CET) which certainly limits the comparability.

4.2 Comparison the temperatures from the UFS lidar and MLS

After initially concentrating just on the co-ordinates of the satellite for a given date (e.g., Klanner et al., 2021) we now also looked at the times of the MLS overpasses, which resulted in a somewhat different view. The mean passage times specified were 1.38 (±0.40) h with respect to noon (CET) and 2.69 (±0.39) h with respect to the following midnight (CET). The "midnight" passages can be expected to be the better choice for the comparisons with the early-night lidar measurements and were normally taken for the statistical evaluation. Morning times on a given day were no longer used. For the downloaded data we consistently found the three latitudes 45.9º N, 47.35º N and 48.8º N which is sufficiently close to UFS (within ±1.6º). By contrast, the longitudes were not reproducible and ranged between 3.2º E and 20.7º E. For just two of the days the longitude perfectly matched that of UFS. However, these profiles did not agree with those from the lidar significantly better. In two cases one measurement time group of MLS was missing, and we took the profile for a passage at a time difference of about ±12 h with respect to midnight.

In addition to Fig. 3 we show in Fig. 4 six examples of comparisons. On average the positive bias of the temperatures from the lidar and that from MLS remained. The best agreement below 70 km is seen in the midnight comparisons (MLS: thin blue lines) in Fig. 3 and Fig. 4e. In three of the cases (not shown in Fig. 4) big positive temperature peaks exceeding the estimated uncertainties could be seen above 70 km in the lidar data. One of these cases is shown in Sect. 4.3. In addition, in Fig. 4f there is a rather excessive deviation between lidar and MLS at 69 km, but here the temperature difference with respect to the MOHp lidar is smaller (thick blue line). Because of the good latitudinal matching this discrepancy is strange. We are unable to explain it. One could think either about wave effects or about an outlier of the lidar measurement. For identifying waves one needs time series which is possible because of the one-hour time resolution of the system.

A very strange deviation was untypically found at rather low altitude for 12 December 2018 (not shown). At the moderate altitude of 46 km the midnight MLS temperature was lower by as much as 25 K than that from the lidar. The difference with respect to the MLS noon temperatures had been just 15 K, also this, however, being out of any expectation for this altitude range. Below 35 km and above 57 km the agreement was reasonable to excellent. For our statistical analysis (see below) we took the noon profile.

In Fig. 5 we show the differences of the profiles for all measurements, as well as the arithmetic average and the positive and negative standard deviation. For the averages we selected the MLS latitude 47.35º N, –0.07º away from that of UFS. In all but two cases the "midnight" MLS profile was taken. The maximum deviations for the lidar are 9.4 K at 52.8 km and 8.6 K at 68.6 km. The minimum difference is found at 61.0 km is 3.1 K. In three profiles the data in a short altitude range below 70 km with excessive deviations were excluded from the averaging.

The negative temperature deviation of MLS confirms the findings in earlier work. Schwartz et al. (2008) compared the MLS temperature profiles with those from several other satellite-borne sensors. They abruptly started to depart from the other profiles above 45 km, the maximum negative offset reaching values between 5 and 8 K. The minimum difference around 60 km is also confirmed. Wing et al. (2018b; 2021) found a similar behaviour for other Rayleigh lidar systems.

4.3 Comparisons of the temperatures from the UFS and MOHp lidar systems

Instead of comparing the UFS results with another satellite-borne sensor such as the proven SABER (Sounding of the Atmosphere using Broadband Emission Radiometry; launch: December 2001; Russell et al., 1999; Mertens et al., 2009; Esplin et al., 2023) we preferred to compare our temperature results with those of the nearby MOHp ozone lidar. The advantage is the mentioned relatively small distance between the two lidar sites

The MOHp temperatures have been demonstrated to match the SABER temperatures almost perfectly (Fig. 10 of Wing et al., 2021), as is the case also for other lidar stations (e.g., Cooper, 2004; Wing et al., 2018b; Dawkins et al., 2018). Thus, we see the MOHp lidar as a suitable reference (see also Steinbrecht et al., 2025). During ~~8~~ 9 of the 14 measurement nights at UFS the MOHp lidar was operated as well. The MOHp temperature are archived above 27 km.

As expected from earlier work (e.g., Wing et al., 2018b; 2021) the UFS and MOHp lidar temperature channels yield a better agreement than the comparisons of the UFS lidar with MLS. However, the temperatures for the two lidar sites may differ. In Fig. 6 the best case is presented with almost identical values up to 71 km (8 November 2021). Above this altitude the UFS temperature profile exhibits a pronounced peak strongly outside the estimated uncertainty above this altitude. The MLS values sometimes deviate strongly which is associated with bad temporal and spatial co-incidence.

The excellent agreement of the lidar results at both stations in Fig. 6 suggests that there is no fundamental mismatch of the retrieval algorithms. Also in Fig. 7 the results do not differ much, except for the range above 66 km. There, the deviation is, still, within the expected uncertainty or the temperature variations suggested by the variability in the GRIPS data. This agreement also suggests the absence of fluorescence effects of the interference filters or PMT issues (see Sect. 5).

However, the examples in Fig. 4 demonstrate that there is, on average, a systematically lower temperature in the MOHp values. This is somewhat surprising because of the good matching of the MOHp temperatures with SABER (Wing et al., 2021) and a similar average offset between SABER and MLS (Schwartz et al., 2008) as found for the UFS lidar in Fig. 5.

At least, the agreement between the two lidar systems is better than that in Fig. 5. This is shown in summary in Fig. 8, prepared in the same way as Fig. 5. The average temperature differences between UFS and MOHp are positive up to almost 80 km, even at the lowest altitudes, where the UFS values agree mostly well with the sonde data (as visible in the examples also down to below 20 km).

This behaviour will be discussed in Sect. 5.

4.4 Comparisons of night-time series at UFS with the MOHp all-night temperature profiles

One issue of comparisons of the lidar measurements at UFS and MOHp is that the measurements at UFS are confined to one hour and were, until 2022, concentrated to the first half of the night, whereas the soundings at MOHP cover full nights. Although on average a night-time temperature increase has been found at the altitude of the OH layer and ascribed to atmospheric tides we speculated on potential night-time cooling of the atmosphere below. Of course, such an effect is difficult to evaluate in the presence of pronounced atmospheric wave activities.

We, therefore, carried out four night-time series in November 2024, i.e., after the end of the period of investigation in the previous sections (February 2022). The measurements were carried out at half-hour intervals with durations of just half an hour, which resulted in a higher variability of the values at high altitudes than for the 1-h measurements. Figure ~~8~~ 9 shows the examples for the last two of the four nights, for which MOHp reference profiles existed and for which the GRIPS temperature variability was low. During these nights the differences of the single-night average UFS and the MOHp temperatures are rather small. Very few profiles depart strongly from the average, beyond our expectations.

In Fig. ~~9~~ 10 we present temperature time series of these two nights for altitudes differing by 5 km between 30 and 80 km. Up to 55 km the series are sufficiently smooth to allow us to judge temperature trends. There is no

indication of major night-time atmospheric cooling over a large altitude range, which is favourable for a good agreement of the two lidar systems. The negative temperature development at 45 km and 50 km during the night between 4 and 5 November could be an exception, but does not exceed the range of the temperature variability. For the other two nights no cooling outside the temperature variability is observed (not shown).

Due to the enhanced noise of the half-hour sounding many lidar temperature profiles could not be evaluated to clearly beyond 80 km. This made the calibration by using the GRIPS values impossible. Nevertheless, we used estimates of the behaviour in the uppermost part of the measurements for a reasonable approach, also looking at the MOHp profiles. Thus, the results above 70 km are somewhat influenced by the reference to GRIPS. As a result of this and because of the smaller number of cases that can be averaged at the highest altitudes the standard deviation diminishes beyond 80 km.

5. Discussion and Conclusions

Klanner et al. (2021) demonstrated that with a powerful XeCl laser and the large receiver Raman backscatter signal accumulated within one hour from atmospheric water can be resolved to more than 25 km during night-time, allowing us to retrieve useful H_2O mixing ratios to at least 20 km. In this study we examine the performance of the Rayleigh temperature channel also for one-hour measurements.

The smoothed backscatter signals of the temperature channel can be discerned from the background up to more than 90 km. Since this corresponds to a small fraction of one count per bin the smoothing must be strong and currently limits the vertical resolution at high altitudes to 2.9 km (as defined in the 1999 VDI guideline). The temperatures can be retrieved starting at several kilometres below this. The retrieval in the uppermost part of the altitude range benefits from the simultaneous OH* measurements at UFS. In cases when the useful range of the lidar ends below 86 km estimates from extrapolations are used.

The rather systematic positive offset of the lidar temperatures with respect to those from MLS between roughly 40 km and 70 km confirms the expectations from earlier work (Schwartz et al., 2008; Medvedeva et al., 2014; Wing et al., 2018b; 2021). As mentioned, other satellite-borne sensors, in particular SABER, have shown an excellent agreement with lidar temperature data above several stations including MOHp.

The agreement of the UFS lidar with the “off” wavelength channel of the MOHp DIAL is better, but on average the UFS temperatures from roughly 45 km to 70 km also deviate positively. However, several profiles agree really well which, together with the agreement below 45 km, suggests that there is no fundamental problem with the retrieval algorithm.

A positive temperature offset means a smaller slope of the air density and, thus, slower decay of the lidar backscatter signal. A slower decay of the backscatter signal would be typical of known technical artefacts that will be discussed below. Since the UFS temperatures are higher than those of MOHp this could suggest that the problems are more on the side of the UFS lidar.

Signal components exhibiting exponential decay are typical artefacts in lidar signal processing. For example, slow fluorescence decay of optical components, in particular of interference filters, could yield slightly higher temperatures above a certain threshold altitude. A threshold behaviour around an altitude of about 40 km is, indeed, observed. However, because of the excellent agreement between the two lidar systems in several cases we hesitate to assume the presence of fluorescence.

In addition, electronic artefacts must be considered. Wing et al. (2018a) attribute positive T biases above 70 km to some extent to electronic cross talk or bursts of transient electronic signals and present a method to discard bad profiles influenced by a shot-by-shot numerical analysis. Such an approach is helpful, but limited to low to

moderate laser repetition rates because of limits in computation speed. In any case, due to sufficient spatial filtering in our receiver our far-field background count rate is of the order of 0.2 h^{-1} bin^{-1} which means negligible interference of bursts. In fact, PMT testing with covered photocathode in the detection system verified even the mostly complete absence of dark counts. The detection system is located far away from sources of electromagnetic interference in a metallic tower outside the building.

Small exponential wings of the backscatter signal that could give rise to higher temperatures can be caused by signal-induced nonlinearities of photomultiplier tubes (Bristow et al., 1996). Two effects must be considered, signal-induced gain change due to overload of the final dynode stages and signal-induced emission of the photocathode. The first type is avoided by limiting the signal, the second one seems to be suppressed in the PMT model chosen to a high degree by kinetic-energy filtering (removal) of the artificial low-energy electrons. Indeed, signal-induced nonlinearities have been found to be absent for the Hamamatsu R7400 detectors under conservative operating conditions, in particular for photon counting (e.g., Trickl et al., 2020; 2024). Kreipl (2006) determined the 1/e decay time of an overloaded R7400-03 cathode to less than 30 µs, i.e., much shorter than the decay time of the backscatter signal of our temperature measurements. These tests had been carried out at a cathode illumination higher by almost two orders of magnitude. In summary, we can exclude signal-induced nonlinearities as the reason of the positive temperature deviations.

There is one important difference between the lidar measurements at UFS and MOHp. The measurements at UFS have taken place before midnight or around midnight the latest. At MOHp, with the exception of the favourable case in Fig. 6, the data acquisition lasted all night, with measurements times up to more than 12 h during the cold season. Atmospheric cooling during the second part of the night could serve as an explanation the observed difference. The GRIPS measurements examined in this study do not reveal reproducible cooling in the mesopause region with progressing night. The GRIPS temperatures tend to grow with time. At lower altitudes (e.g.) the examples of Kopp et al. (2015) do not allow us to resolve a temperature change because of the wave structure superimposed on the temperature profiles. At least our night-time measurement series in November 2024 demonstrate in these cases that in the almost complete absence of atmospheric cooling the temperature differences obtained at UFS and MOHp stay strongly below the variability of the 0.5-h UFS lidar data.

A bias caused by misalignment can be excluded since this would lead to deviations at low altitudes. This kind of problem has been limited to altitudes below 20 km.

Apart from these issues a range extension to more than 105 km is desirable since this would allow us to retrieve temperatures with uncertainties of the order of ±5 K up to almost 90 km, which covers the well-mixed part of the atmosphere (U.S. Standard Atmosphere, 1976). The GRIPS measurement range would then be included in the useful operating range of the lidar and the temperature obtained from the spectra could be controlled by vertical sounding. As one can judge from Fig. 1 such a range extension would require a ten times higher laser power. Since the pulse energy of the current laser is adequate for not exceeding signal levels that ensure linear detection a much higher pulse repetition rate would be the solution. Diode-laser-pumped Nd:YAG with similar third-harmonic pulse energies but a repetition rate of more than 300 Hz are meanwhile commercially available. 300 Hz would match the repetition rate of the XeCl laser and water vapour and temperature measurements could be made simultaneously, with delayed pulses in order to minimize spectral interference. This would mean 15 times the power of the current transmitter.

In three cases we observed excessive temperature peaks around and above 70 km. Because of the low signal level at these altitudes we cannot exclude signal outliers which, again, calls for a higher backscatter signal.

However, temperature excursions of the order of 20 K in the mesopause region have been presented in earlier work and attributed to waves (e.g., Kopp et al., 2015). A clear identification of gravity waves requires to carry out our time series with a better signal-to-noise ratio.

In addition, an influence of particles or fluorescence from meteorites must be distinguished. One example of a potential particle layer observed at 54 km with our stratospheric aerosol lidar (Trickl et al., 2013; 2024) is given in Fig. ~~10~~11. An identification of the presence of particles cannot be achieved with a simple backscatter lidar. The particle contribution can be removed by spectral filtering the scattered light from a narrowband frequency-doubled Nd:YAG laser in iodine (Piironen and Eloranta et al., 1994) . For our system we could think of additional measurements at the also available 532.2-nm laser emission with an iodine filter as successfully implemented in our mobile aerosol lidar before (Giehl and Trickl, 2010; Wandinger et al., 2016). The problem of the light absorption in ozone at 532.2 nm does not matter at high altitudes.

The advantage of symbiotic use of the GRIPS observations at UFS could be strengthened by adding a vertically pointing spectrometer. In the near future, the current set-up with two identical spectrometers will be extended by a third spectrometer that will be aligned for parallel measurements with the laser beam. This, together with less noisy lidar data, would simplify the interpretation of remaining differences. More detailed studies of the airglow layer could be made by tuning the fundamental wavelength of the Raman lidar wavelength to 308.15 nm where OH laser-induced fluorescence can be excited (Brinksma et al., 1998).

After the completion of the upgrading the beginning of routine lidar measurements is planned, as a potential contribution to NDACC.

5 Data availability

Lidar data from the UFS lidar can be obtained from the authors, but are currently flagged as preliminary. GRIPS temperatures are available at https://zenodo.org/records/15267440. MLS v5 temperature data are available at https://disc.gsfc.nasa.gov/datasets?page=1&keywords=ML2T_005/. A full list of MLS data can be found at http://disc.sci.gsfc.nasa.gov/Aura/dataholdings/. The MOHp lidar data can be freely downloaded from the NDACC data base (https://www-air.larc.nasa.gov/missions/ndacc/data.html).

6 Author statement

TT and HV carried out and evaluated the UFS lidar measurements. MB, CS and SW are responsible for the GRIPS observations, WS for the lidar measurements at MOHp. GN preselected and provided the MLS data. All authors contributed to preparing this manuscript.

7 Competing interests

The authors declare that they have no conflict of interest.

Acknowledgements

The authors from IMK-IFU thank Hans Peter Schmid for his support. Lisa Klanner (until 2015) and Matthias Perfahl strongly contributed to the technical development of the system that recently has included remote control. We are indepted to the considerable assistance of the UFS staff. The lidar development was funded by the Bavarian Staatsministerium für Umwelt und Verbraucherschutz (BayStMUV). The GRIPS observations at UFS have also been supported by BayStMUV in projects including GUDRUN, grant no. 71b-U8729-2003/125-13; GRIPS3 Back-Up, 2009/40051; BHEA, TLK01U-49580; LUDWIG, TUS01UFS-67093; VoCaS,

TKP01KPB-70581; and AlpEn-DAC, TUS01UFS-72184). Gerald Nedoluha was supported by the NASA Earth Sciences Division Upper Atmosphere Research Program and by the Office of Naval Research.

The service charges for this open access publication have been covered by a Research Centre of the Helmholtz Association.

References

Alpers, M., Eixmann, R., Fricke-Begemann, C., Gerding, M., and Höffner, J.: Temperature lidar measurements from 1 to 105 km altitude using resonance, Rayleigh, and Rotational Raman Scattering. Atmos. Chem. Phys., 4,793–800, 2004.

Arnold, K. S., and She, C. Y.: Metal fluorescence lidar (light detection and ranging) and the middle atmosphere, Contemp. Phys., 44, 35 – 49, 2003.

Arshinov, Y. F., Bobrovnikov, S. M., Zuev, V. E., and Mitev, V. M.: Atmospheric temperature measurements using a pure rotational Raman lidar, Appl. Optics, 22, 2984–2990, 1983.

Baker, D. J. and Stair, A. T.: Rocket measurements of the altitude distributions of the hydroxyl airglow, Physica Scripta, 37, 611–622, https://doi.org/10.1088/0031-8949/37/4/021, 1988.

Behrendt, A.: Temperature Measurements with Lidar, pp. 273-305 in: Lidar – Range-Resolved Optical Remote Sensing of the Atmosphere, Claus Weitkamp, Ed., Springer Science and Business Media (New York, U.S.A.), ISBN 0-387-40075-3, 2005.

Beig, G., Keckhut, P., Lowe, R. P., Roble, R. G., Mlynczak, M. G., Scheer, J., Fomichev, V. I., Offermann, D., French, W. J. R., Shepherd, M. G., Semenov, A. I., Remsberg, E. E., She, C. Y., Lübken, F. J., Bremer, J., Clemesha, B. R., Stegman, J., Sigernes, F., and Fadnavis, S.: Review of mesospheric temperature trends, Rev. Geophys., 41, RG1015, https://doi.org/10.1029/2002RG000121, 2003.

Bittner, M., Offermann, D., and Graef, H. H.: Mesopause temperature variability above a midlatitude station in Europe, J. Geophys. Res., 105, 2045-2058, 2000.

M. Bittner, M., Offermann, D., Graef, H.-H., Donner, M., and Hamilton, K.: An 18-year time series of OH rotational temperatures and middle atmosphere decadal variations, J. Atmos. Solar-Terr. Phys., 64, 1147–1166, 2002.

Blamont, J. E., Chanin, M. L., and Mégie, G.: Vertical distribution and temperature profile of night time sodium layer obtained by laser backscatter, Ann. Geophys., 26**,** 833-838, 1972.

Bowman, M. R., Gibson, A. J., and Sandford, M. C. W.: Atmospheric Sodium measured by a Tuned Laser Radar, Nature, 221, 456-457, 1969.

Brinksma, E. J., Meijer, Y. J., McDermid, I. S., Cageao, R. P., Bergwerf, J. B., Swart, D. P. J., Ubachs, W., Matthews, W. A., Hogervorst, W., and Hovenier, J. W.: First lidar observations of mesospheric hydroxyl, Geophys. Res. Lett., 25, 51-54, 1998; erratum: Geophys Res. Lett., 25, 521, 1998.

Bristow, M. P., Bundy, D. H., and Wright, A. G.: Signal linearity, gain stability, and gating in photomultipliers: application to differential absorption lidars, Appl. Opt., 34, 4437-4452, 1996.

Carnuth, W., Kempfer, U., and Trickl, T.: Highlights of the tropospheric lidar studies at IFU within the TOR project, Tellus B, 54, 163-185, 2002.

Chen, H., White, M. A., Krueger, D. A., and She, C. Y.: Daytime mesopause temperature measurements with a sodium-vapor dispersive Faraday filter in a lidar receiver, Opt. Lett., 21, 1093-1095, 1996.

Chu, X., Gardner, C. S., and Papen, G.: Lidar Observations of Polar Mesospheric Clouds at South Pole: Diurnal Variations, Geophys. Res. Lett., 28, 1937-1940, 2001.

Cooper, M.: Validation of SABER Temperature Measurements Using Ground-based Instruments, IGARSS 2004. 2004 IEEE International Geoscience and Remote Sensing Symposium, IEEE Xplore, https://doi.org/10.1109/IGARSS.2004.1370033, 2004.

Curtis, R. D., Houghton, J. T., Peskett, G. D., and Rodgers, C. D.: The pressure modulator radiometer for Nimbus F, Proc. R. Soc. London, A 337, 135-150, 1974.

Dawkins, E. C. M., Feofilov, A., Rezac, L., Kutepov, A. A., Janches, D., Höffner, J., Chu, X., Lu, X., Mlynczak, M. G., and Russell, J. III: Validation of SABER v2.0 operational temperature data with ground-based lidars in the mesosphere-lower thermosphere region (75–105 km). J. Geophys. Res., 123, 9916–9934, 2018.

Englert, C. R., Stevens, M. H., Siskind, D.- E., Harlander, J. M., and Roesler, F. L.: Spatial Heterodyne Imager for Mesospheric Radicals on STPSat□1, J. Geophys. Res., 115, D20306, doi:10.1029/2010JD014398, 20 pp., 2010.

Esplin, R., Mlynczak, M. G., Russell, J., Gordley, L., and The SABER Team: Sounding of the Atmosphere using Broadband Emission Radiometry (SABER): Instrument and Science Measurement Description, Earth and Space Science, 10, e2023EA002999, 32 pp., 2023.

Fishbein, E. F., Cofield, R. E., Froidevaud, L., Jarnot, R. F., Lungu, I. T., Read, W. G., Shippony, Z., Waters, J. W., McDermid, I. S., McGee, T. J., Singh, U., Gross, M., Hauchecorne, A., Keckhut, P., Gelman, M. E., and Nagatani, R. M.: Validation of UARS Microwave Limb Sounder temperature and pressure measurements, J. Geophys. Res., 101, 9983-10016, 1996; the paper includes 353-nm measurements of the Table Mountain Facility (McDermid et al., 1990).

Fricke, K. H., and von Zahn, U.: Mesopause temperatures derived from probing the hyperfine structure of the D_2 resonance line of sodium by lidar, J. Atmos. Terr. Phys., 47, 499-512, 1985.

Gerding, M., Höffner, J., Kopp, M., Eixmann, R., and Lübken, F.-J.: Mesospheric temperature and aerosol soundings during day and night: spectra land spatial filtering techniques. in: 25th International Laser Radar Conference, St. Petersburg, Russia, 2010, pp. 67–70, 2010.

Giehl, H., and Trickl, T.: Testing the IFU High-Spectral-Resolution Lidar at the 2009 Leipzig Field Campaign, pp. 920-923 in: Proceedings of the 25th International Laser Radar Conference, St.-Petersburg (Russia), July 5 to 9, 2010, G. Matvienko, A. Zemlyanov, Eds., V. E. Zuev Institute of Optics (Tomsk, Russia), 2010.

Gille, S. T., Hauchecorne, A., and Chanin, M.-L.: Semidiurnal and diurnal tidal effects in the middle atmosphere as seen by Rayleigh lidar, J. Geophys. Res., 96, 7579-7587, 1991.

Granier, C., Jegou, J. P., and Mégie, G.: Iron Atoms and Metallic Species in the Earth´s upper Atmosphere, Geophys. Res. Lett., 16, 243-246, 1989.

671 Hannawald, P., Schmidt, C., Sedlak, R., Wüst, S., and Bittner, M.: Seasonal and intra-diurnal variability of
672 small-scale gravity waves in OH airglow at two Alpine stations, Atmos. Meas. Tech., 12, 457–469, 2019

673 Hauchecorne, A., and Chanin, M.-L.: Density and Temperature Profiles Obtained by Lidar between 33 and 70
674 km, Geophys. Res. Lett., 7, 565-568, 1980.

675 Hauchecorne, A., Chanin, M.-L., and Keckhut, P.: Climatology and Trends of the Middle Atmospheric
676 Temperature (33–87 km) as Seen by Rayleigh Lidar over the South of France, J. Geophys. Res., 96, 15297-
677 15309, 1991.

678 Höffner, J., and Lautenbach, J.: Daylight measurements of mesopause temperature and vertical wind with the
679 mobile scanning iron lidar, Opt. Lett. 34, 1351-1353 (2009)

680 Höveler, K.: Entwicklung eines Nahbereichsempfängers zur Messung von Wasserdampf- und Temperaturpro-
681 filen für das Hochleistungs-Raman-Lidar am Schneefernerhaus, Masterarbeit, Karlsruher Institut für
682 Technologie, Fakultät für Physik, 138 pp., 2015 (in German).

683 Iarlori, M., Madonna, F., Rizi, V., Trickl, T., and Amodeo, A.: Effective resolution concepts for lidar
684 observations, Atmos. Meas. Tech., 8, 5157–5176, https://doi.org/10.5194/amt-8-5157-2015, 2015.

685 Jäger, H. and Deshler, T.: Lidar backscatter to extinction, mass and area conversions for stratospheric aerosols
686 based on midlatitude, Geophys. Res. Lett., 29, 1929, 2002.

687 Jäger, H. and Deshler, T.: Correction to "Lidar backscatter to extinction, mass and area conversions for
688 stratospheric aerosols based on midlatitude balloonborne size distribution measurements", Geophys. Res. Lett.,
689 30, 1382, 2003.

690 Keckhut, P.: Middle atmospheric temperature measurements with lidar, J. Physique, 121**,** 239–248, 2004.

691 Khanna, J., Bandoro, J., Sica, R. J., and McElroy, C. T.: New technique for retrieval of atmospheric temperature
692 profiles from Rayleigh-scatter lidar measurements using nonlinear inversion, Appl. Opt., 51, 7945-7852, 2012.

693 Kim, Y.-J., Eckermann, S. D., and Chun, H.-Y.: An overview of the past, present and future of gravity□wave
694 drag parametrization for numerical climate and weather prediction models. Atmosphere-Ocean, 41, 65-98, 2003.

695 Klanner, L.: Entwicklung eines Hochleistungs-Raman-Lidars für die Messung von Wasserdampf- und
696 Temperaturprofilen in der Atmosphäre, Technische Universität München, Fakultät Wissenschaftszentrum
697 Weihenstephan, Dissertation, 186 pp., 2022 (in German).

698 Klanner, L., Höveler, K., Khordakova, D., Perfahl, M., Rolf, C., Trickl, T., and Vogelmann, H.: A powerful lidar
699 system capable of 1 h measurements of water vapour in the troposphere and the lower stratosphere as well as the
700 temperature in the upper stratosphere and mesosphere, Atmos. Meas. Tech., 14, 531-555, 2021.

701 Klett, J. D.: Stable analytical inversion solution for processing lidar returns, Appl. Opt., 20, 211-220, 1981.

702 Klett, J. D.: Lidar inversion with variable backscatter/extinction ratios, Appl. Opt., 24, 1638-1643, 1985.

703 Kopp, M., Gerding, M., Höffner, J., and Lübken, F.-J.: Tidal signatures in temperatures derived from daylight
704 lidar soundings above Kühlungsborn (54°N, 12°E), J. Atmos. Sol.-Terr. Phys., 127, 37–50, 2015.

705 Kreipl, S.: Messung des Aerosoltransports am Alpennordrand mittels Laserradar (Lidar), Dissertation, Friedrich-
706 Alexander-Universität Erlangen-Nürnberg (Germany), 195 pp., 2006 (in German); the relevant figure can be
707 found at http://www.trickl.de/PMT.PDF.

Leblanc, T., McDermid, I. S., Keckhut, P., Hauchecorne, A., She, C. Y., and Krueger, D. A.: Temperature climatology of the middle atmosphere from long-term lidar measurements at middle and low latitudes, J. Geophys. Res., 103, 17191-17204, 1998

Leblanc, T., Sica, R. J., van Gijsel, J. A. E., Godin-Beekmann, S., Haefele, A., Trickl, T., Payen, G., and Gabarrot, F.: Proposed standardized definitions for vertical resolution and uncertainty in the NDACC lidar ozone and temperature algorithms – Part 1: Vertical resolution, Atmos. Meas. Tech., 9, 4029–4049, https://doi.org/10.5194/amt-9-4029-2016, 2016.6.

Liu, G. and Shepherd, G. G.: An empirical model for the altitude of the OH nightglow emission, Geophys. Res. Lett., 33, L09805, https://doi.org/10.1029/2005gl025297, 2006.

Li, A., Roth, C. Z., Bourassa, A. E., Degenstein, D. A., Pérot, K., Christensen, O. M., and Murtagh, D. P.: The OH (3-1) nightglow volume emission rate retrieved from OSIRIS measurements: 2001 to 2015. Earth Syst. Sci. Data, 13(11), 5115-5126, https://doi.org/10.5194/essd-13-5115-2021, 2021.

Lopez-Moreno, J. J., Rodrigo, R., Moreno, F., Lopez-Puetas, M., and Molina, A.: Altitude distribution of vibrationally excited states of atmospheric hydroxyl at levels v = 2 to v = 7, Planet. and Space Sci., 35(8), 1029-1038, https://doi.org/10.1016/0032-0633(87)90007-9, 1987.

McDermid, I. S., Godin, S. M., and Walsh, T. D.: Lidar measurements of stratospheric ozone and intercomparisons and validation, Appl. Opt., 29, 4914-4923, 1990.

Medvedev, A. S., and Yiğit, E.: Gravity waves in planetary atmospheres: Their effects and parameterization in global circulation models. Atmosphere, 10, 531, 2019.

Medvedewa, I. V., Semenov, A. I., Perminov, V. I., Beletsky, A. B., and Tartarnikov, A. V.: Comparison of Ground-based OH Temperature Data Measured at Irkutsk (52°N, 103°E) and Zvenigorod (56°N, 37°E) Stations with Aura MLS v3.3, 62, pp. 340-349, DOI: 10.2478/s11600-013-0161-x, 2014.

Mégie, G., Bos, F., Blamont, J. E., and Chanin, M. L.: Simultaneous Nighttime Measurements of Sodium and Potassium, Planet. Space Sci., 26, 27-35, 1978.

Mertens, C. J., Russell, J. M. III, Mlynczak, M. G., She, C,-Y., Schmidlin, F. J., Richard A. Goldberg, R. A., López-Puertas, M., Wintersteiner, P. P., Picard, R. H., Winick, J. R., and Xu, X.: Kinetic temperature and carbon dioxide from broadband infrared limb emission measurements taken from the TIMED/SABER instrument, Adv. Space Res., 43, 15–27, 2009.

Mulligan, F., Horgan, D., Galligan, J., and Griffin, E.: Mesopause temperatures and integrated band brightnesses calculated from airglow OH emissions recorded at Maynooth (53.2° N, 6.4° W) during 1993, J. Atmos. Terr. Phys., 57, 1623–1637, 1995.

Mohr, P. J., Newell, D. B., and Taylor, B. N.: CODATA recommended values of the fundamental physical constants: 2014, Rev. Modern Phys., 88, 035009, 73 pp., 2016.

Nedoluha, G. E. , Gomez, R. M., Boyd, I. , Neal, H., Allen, D. R., and Lambert, A.: The Spread of the Hunga Tonga H_2O Plume in the Middle Atmosphere Over the First Two Years Since Eruption, J. Geophys. Res., 129, e2024JD040907. https://doi.org/10. 1029/2024JD0409, 11 pp., 2024.

Nedoluha, G. E. , Gomez, R. M., Boyd, I. , Neal, H., Allen, D. R., Parrish, A., Connor, B.- J., and Siskind, D. E.: Measurements of Stratospheric ClO From Mauna Kea: 1992–2023, J. Geophys. Res., 130, e2024JD041848. https://doi.org/10.1029/2024JD041848, 13 pp., 2025.

747 Noll, S., Kimeswenger, S., Proxauf, B., Unterguggenberger, S., Kausch, W., and Jones, A. M.: 15 years of
748 VLT/UVES OH intensities and temperatures in comparison with TIMED/SABER data, J. Atmos. Sol.-Terr.
749 Phys., 163, 54–69, 2017.

750 Noll, S., Winkler, H., Goussev, O., and Proxauf, B.: OH level populations and accuracies of Einstein-A
751 coefficients from hundreds of measured lines, Atmos. Chem. Phys., 20, 5269–5292, 2020.

752 Noll, S., Schmidt, C., Kausch, W., Bittner, M., and Kimeswenger, S.: Climatologies of various OH lines from
753 about 90,000 X-shooter spectra, J. Geophys. Res., 128, https://doi.org/10.1029/2022JD038275, 2023.

754 Ott, H.: Single atom detection in ultracold quantum gases: a review of current progress, Rep. Prog. Phys., 79,
755 054401, 2016.

756 Papen, G. C., Pfenninger, W. M., and Simonich, D. M.: Sensitivity analysis of Na narrowband wind-temperature
757 lidar systems, Appl. Opt., 34, 480-498, 1995.

758 Piironen, P., and Eloranta, E. W.: Demonstration of a high-spectral-resolution lidar based on an iodine
759 absorption filter, Opt. Lett., 19, 234-236, 1994.

760 Reisin, E. R., Scheer, J., Dyrland, M. E., Sigernes, F., Deehr, C. S., Schmidt, C., Höppner, K., Bittner, M.,
761 Ammosov, P. P., Gavrilyeva, G. A., Stegman, J., Perminov, V. I., Semenov, A. I., Knieling, P., Koppmann, R.,
762 Shiokawa, K., Lowe, R. P., López-González, M. J., Rodríguez, E., Zhao, Y., Taylor, M. J., Buriti, R. A., Espy, P.
763 J., French, W. J. R., Eichmann, K.-U., Burrows, J. P., and von Savigny, C.: Traveling planetary wave activity
764 from mesopause region airglow temperatures determined by the Network for the Detection of Mesospheric
765 Change (NDMC), J. Atmos. Sol.-Terr. Phys., 119, 71–82, 2014.

766 Russell, J. M. III, Mlynczak, M. G., Gordley, L. L., Tansock, J., and Esplin, R.: An overview of the SABER
767 experiment and preliminary calibration results, Proc. SPIE, 3756, 277-288, 1999.

768 Scheer, J., Reisin, E. R., Espy, J. P., Bittner, M., Graef, H. H., Offermann, D., Ammoso, P. P., and Ignatyev, V.
769 M.: Large-scale structures in hydroxyl rotational temperatures during DYANA, J. Atmos. Terr. Phys., 56, 1701-
770 1715, 1994.

771 Schmidt, C., Höppner, K., and Bittner, M.: A ground-based spectrometer equipped with an InGaAs array for
772 routine observations of OH (3-1) rotational temperatures in the mesopause region, J. Atmos. Sol.-Terr. Phys.,
773 102, 125–139 2013.

774 Schmidt, C., Dunker, T., Lichtenstern, S., Scheer, J., Wüst, S., Hoppe, U.-P., and Bittner M.: Derivation of
775 vertical wavelengths of gravity waves in the MLT-region from multispectral airglow observations, J. Atmos.
776 Sol.-Terr. Phys., 173, 119-127, https://doi.org/10.1016/j.jastp.2018.03.002, 2018.

777 Schmidt, C., Küchelbacher, L., Wüst, S., and Bittner, M.: OH airglow observations with two identical
778 spectrometers: benefits of increased data homogeneity in the identification of variations induced by the 11-year
779 solar cycle, the QBO, and other factors. Atmos. Meas. Tech. 16, 4331-4356, https://doi.org/10.5194/amt-16-
780 4331-2023, 2023.

781 Schoeberl, M. R., Douglass, A. R., Hilsenrath, E., Bhartia, P. K., Beer, R., Waters, J. W., Gunson, M. R.,
782 Froidevaux, L., Gille, J. C., Barnett, J. J., Levelt, P. F., and DeCola, P.: Overview of the EOS Aura mission,
783 IEEE Trans. Geosci. Remote Sens., 44, 1066–1074, 2006.

784 Schwartz, M. L., Lambert, A., Manney, G. L:, Read, W. G., Livesey, N. E., J., Froidevaux, L., Ao, C. O.,
785 Bernath, P. F., Boone, C. D., Cofield, R. E., Daffer, W. H., Drouin, B. J., Fetzer, E. J., Fuller, R. A., Jarnot, R.
786 F., Jiang, J. H., Jiang, Y. B., Knosp, B. W., Krüger, K., Li, J.-L. F., Mlynczak, M. G., Pawson, S., Russell, J. M.
787 III, Santee, M. L., Snyder, W. V., Stek, P. C., Thurstans, R. P., Tompkins, A. M., Wagner, P. A., Walker, K. A.,
788 Waters, J. W., and Wu, D. L.: Validation of the Aura Microwave Limb Sounder temperature and geopotential
789 height measurements, J. Geophys. Res., 113, D15S11, doi: 10.1029/2007JD008783, 23 pp., 2008.

790 Serikov, I., and Bobrinikov, S.: Atmospheric temperature profiling with pure rotational Raman lidars, pp. 149-
791 216, Series: Optoelectronic Materials and Devices, Vol. 7, Recent Advances in Atmospheric Lidars, L. Fiorani,
792 and V. Mitev, Eds., National Institute of Research and Development for Optoelectronics (Bucharest, Romania),
793 ISBN 978-973-88109-6-9, 2009.

794 She, C. Y., and Lowe, R.P.: Seasonal temperature variations in the mesopause region at mid-latitudes:
795 Comparison of lidar and hydroxyl rotational temperatures using WINDII/UARS OH height profiles, J. Atmos.
796 Solar-Terr. Phys., 60, 1573–1583, 1998.

797 She, C. V., Lativi, H., Yu, Y. R., Alvarez II, R. J., Bills, R. E., and Gardner, C. S.: Two-frequency Lidar
798 Technique for Mesospheric Na Temperature Measurements, Geophys. Res. Lett., 17, 929-932, 1990.

799 Shibata, T., Kobuchi, M., and Maeda, M.: Measurements of density and temperature profiles in the middle
800 atmosphere with a XeF lidar, Appl. Optics, 25, 685–688, 1986.

801 Sica, R. J., Measurements of the Effects of Gravity Waves in the Middle Atmosphere Using Parametric Models
802 of Density Fluctuations. Part II: Energy Dissipation and Eddy Diffusion, J. Atmos. Sci., 56, 1330-1343, 1999.

803 Sica, R. J., Sargoytchev, S., Argall, P. S., Borra, E. F., Girard, L., Sparrow, C. T., and Flatt, S.: Lidar
804 measurements taken with a large-aperture liquid mirror. 1. Rayleigh-scatter system, Appl. Opt., 34, 6925-6936,
805 1995.

806 Sivjee, G. G.: Airglow Hydroxyl Emissions, Planet. Space Sci., 40, 235–242, 1992.

807 Steinbrecht, W ., Velazco, V. A., Dirksen, R., Doppler, L., Oelsner, P., Van Malderen, R., De Backer, H.,
808 Maillard Barras, E., Stübi, R., Godin-Beekmann, S., and Hauchecorne, A.: Ground-Based Monitoring of
809 Stratospheric Ozone and Temperature Over Germany Since the 1960s, Earth Space Sci., 12, e2024EA003821, 24
810 pp., https://doi.org/10.1029/2024, 2025.

811 Takahashi, H., Clemesha, B. R., Simonich, D. M., Melo, S. M. L., Teixeira, N. R., Eras, A., Stegman, J., Witt,
812 G.: Rocket measurements of the equatorial airglow: MULTIPHOT 92 database, J. Atmos. Terr. Phys., 58, 1943–
813 1961, 1996.

814 Trickl, T.: Upgraded 1.56-µm lidar at IMK-IFU with 0.28 J/pulse, Appl. Opt., 49, 3732-3740, 2010.

815 Trickl, T., Giehl, H., Jäger, H., and Vogelmann, H.: 35 years of stratospheric aerosol measurements at Garmisch-
816 Partenkirchen: from Fuego to Eyjafjallajökull, and beyond, Atmos. Chem. Phys., 13, 5205-5225, 2013.

817 Trickl, T., Vogelmann, H., Giehl, H., Scheel, H. E., Sprenger, M., and Stohl, A.: How stratospheric are deep
818 stratospheric intrusions? Atmos. Chem. Phys., 14, 9941-9961, 2014.

819 Trickl, T., Vogelmann, H., Flentje, H., and Ries, L.: Stratospheric ozone in boreal fire plumes – the 2013 smoke
820 season over Central Europe, Atmos. Chem. Phys., 15, 9631-9649, 2015.

Trickl, T., Vogelmann, H., Fix, A., Schäfler, A., Wirth, M., Calpini, B., Levrat, G., Romanens, G., Apituley, A., Wilson, K. M., Begbie, R., Reichardt, J., Vömel, H. and Sprenger, M.: How stratospheric are deep stratospheric intrusions into the troposphere? LUAMI 2008, Atmos. Chem. Phys, 16, 8791-8815, 2016.

Trickl, T., Neidl, F., Giehl, H., Perfahl, M., and Vogelmann, H.: Three decades of tropospheric ozone lidar development at Garmisch-Partenkirchen, Atmos. Meas. Tech., 13, 6357-6390, 2020.

Trickl, T., Adelwart, M., Khordakova, D., Ries, L., Rolf, C., Steinbrecht, W., and Vogelmann, H.: Local comparisons of tropospheric ozone: Vertical sounding at two neighbouring stations in Southern Bavaria, Atmos. Meas. Tech. 16, 5145–5165. 2023.

Trickl, T., Vogelmann, H., Fromm, M. F., Jäger, H., Perfahl, M., and Steinbrecht, W.: Measurements report: Violent biomass burning and volcanic eruptions: a new period of elevated stratospheric aerosol over Central Europe (2017 to 2023) in a long series of observations, Atmos. Chem. Phys., 24, 1997-2021, 2024.

U.S. Standard Atmosphere: National Oceanic and Atmospheric Organization (NOAA), National Aeronautics and Space Administration, United States Air Force, NOAA-S/T 76-1562, US Printing Office (Washington, D.C.), 227 pp., 1976.

VDI: guide line 4210 Remote Sensing, Atmospheric Measurements with LIDAR, Measuring gaseous air pollution with the DAS LIDAR, Verein Deutscher Ingenieure, Düsseldorf, Germany, 47 pp., 1999.

Vogelmann, H. and Trickl, T.: Wide-Range Sounding of Free-Tropospheric Water Vapor with a Differential-Absorption Lidar (DIAL) at a High-Altitude Station, Appl. Opt., 47, 2116-2132, 2008.

Vogelmann, H., Sussmann, R., Trickl, T., and Borsdorff, T.: Intercomparison of atmospheric water vapor soundings from the differential absorption lidar (DIAL) and the solar FTIR system on Mt. Zugspitze, Atmos. Meas. Tech., 4, 835-841, 2011.

Von Savigny, C., McDade, I. C., Eichmann, K.-U., and Burrows, J. P.: On the dependence of the OH* Meinel emission altitude on vibrational level: SCIAMACHY observations and model simulations, Atmos. Chem. Phys., 12, 8813–8828, 2012.

Von Savigny, C. and Lednyts'kyy, O.: On the relationship between atomic oxygen and vertical shifts between OH Meinel bands originating from different vibrational levels, Geophys. Res. Lett. 40, 5821–5825. https://doi.org/10.1002/2013GL058017, 2013.

Von Zahn, U., Fricke, K. H, Gerndt, R., and Blix, T.: Mesospheric temperatures and the OH layer height as derived from ground-based lidar and OH* spectrometry, J. Atmos. Terr. Phys., 38, 49, 863–869, 1987.

Von Zahn, U., von Cossart, G., Fiedler, J., Fricke, K. H., Nelke, G., Baumgarten, G., Rees, D., Hauchecorne, A., and Adolfsen, K.: The ALOMAR Rayleigh/Mie/Raman lidar: objectives, configuration, and performance, Ann. Geophysicae, 18, 815-833, 2000.

Waters, J. W., Froidevaux, L., Harwood, R. S., Jarnot, R. F., Pickett, H. M., Read, W. G., Siegel, P. H., Cofield, R. E., Filipiak, M. J., Flower, D. A., Holden, J. R., Lau, G. K., Livesey, N. J., Manney, G. L., Pumphrey, H. C., Santee, M. L., Wu, D. L., Cuddy, D. T., Lay, R. R. Loo, M. S., Perun, V. S., Schwartz, M. J., Stek, P. C., Thurstans, R. P., Boyles, M. A., Chandra, K. M., Chavez, M. C., Chen, G.-S., Chudasama, B. V., Dodge, R., Fuller, R. A., Girard, M. A., Jiang, J. H., Jiang, Y. Knosp, B. W., LaBelle, R. C., Lam, J. C., Lee, K. A., Miller, D., Oswald, J. E., Patel, N. C., Pukala, D. M., Quintero, O., Scaff, D. M., Van Snyder, W. Tope, M. C., Wagner,

P. A., and Walch M. J.: The Earth Observing System Microwave Limb Sounder (EOS MLS) on the Aura satellite, IEEE Trans. Geosci. Remote Sens., 44, 1075–1092, 2006.

Wandinger, U., Freudenthaler, V., Baars, H., Amodeo, A., Engelmann, R., Mattis, I., Groß, S., Pappalardo, G., Giunta, A., D'Amico, G., Chaikovsky, A., Ossipenko, F., Slesar, A., Nicolae, D., Belegante, L., Talianu, C., Serikov, I., Linné, H., Jansen, F., Apituley, A., Wilson, K., de Graaf, M., Trickl, T., Giehl, H., Adam, M., Comeron, A., Muñoz-Porcar, C., Rocadenbosch, F., Sicard, M., Tomás, S., Lange, D., Kumar, D., Pujadas, M., Molero, F., Fernandez, A. J., Alados Arboledas, L., Bravo-Aranda, J. A., Navas-Guzmán, F., Guerrero-Rascado, J, L., Granados-Munoz, M. J.. Preißler, J., Wagner, F., Gausa, M., Grigorov, I., Stoyanov, D., Iarlori, M., Rizi, V., Spinelli, N., Boselli, A., Wang, X., Lo Feudo, T., Perrone, M. R., De Tomasi, F., and Burlizzi, P.: EARLINET instrument intercomparison campaigns: Overview on strategy and results, Atmos. Meas. Tech., 9, 1001-1023, 2016.

Wing, R., Hauchecorne, A., Keckhut, P., Godin-Beekmann, S., Khaykin, S., McCullough, E. M., Mariscal, J.-F. and d'Almeida, E.: Lidar temperature series in the middle atmosphere as a reference data set – Part 1: Improved retrievals and a 20-year cross-validation of two co-located French lidars, Atmos. Meas. Tech., 11, 5531–5547, 2018a.

Wing, R., Hauchecorne, A., Keckhut, P., Godin-Beekmann, S., Khaykin, S., and McCullough, E. M.: Lidar temperature series in the middle atmosphere as a reference data set – Part 2: Assessment of temperature observations from MLS/Aura and SABER/TIMED satellites, Atmos. Meas. Tech., 11, 6703–6717, 2018b.

Wing, R., Godin-Beekmann, S., Steinbrecht, W., McGee, T. J., Sullivan, J. T., Khaykin, S., Sumnicht, G., and Twigg, L.: Evaluation of the new DWD ozone and temperature lidar during the Hohenpeißenberg Ozone Profiling Study (HOPS) and comparison of results with previous NDACC campaigns, Atmos. Meas. Tech., 14, 3773–3794, 2021

Wüst, S., Bittner, M., Yee, Y.-H., Mlynczak, M. G., and Russell, J. M. III: Variability of the Brunt–Väisälä frequency at the OH* layer height, Atmos. Meas. Tech., 10, 4895–4903, https://doi.org/10.5194/amt-10-4895-2017, 2017.

Wüst, S., Bittner, M., Yee, J.-H., Mlynczak, M. G., and Russell III, J. M.: Variability of the Brunt–Väisälä frequency at the OH∗-airglow layer height at low and midlatitudes, Atmos. Meas. Tech., 13, 6067–6093, https://doi.org/10.5194/amt-13-6067-2020, 2020.

Wüst, S., Bittner, M., Espy, P. J., French, P. J., and Mulligan, F.- J.: Hydroxyl airglow observations for investigating atmospheric dynamics: results and challenges, Atmos. Chem. Phys., 23, 1599-1618, https://doi.org/10.5194/acp-23-1599-2023, 2023.

Xu, J., She, C. Y., Yuan, W., Mertens, C., Mlynczak, M., and Russell, J.: Comparison between the temperature measurements by TIMED/SABER and lidar in the midlatitude, J. Geophys. Res., 111, A10S09, doi: 10.1029/2005JA011439, 11pp., 2006.

894 **Figures:**

895

896

897

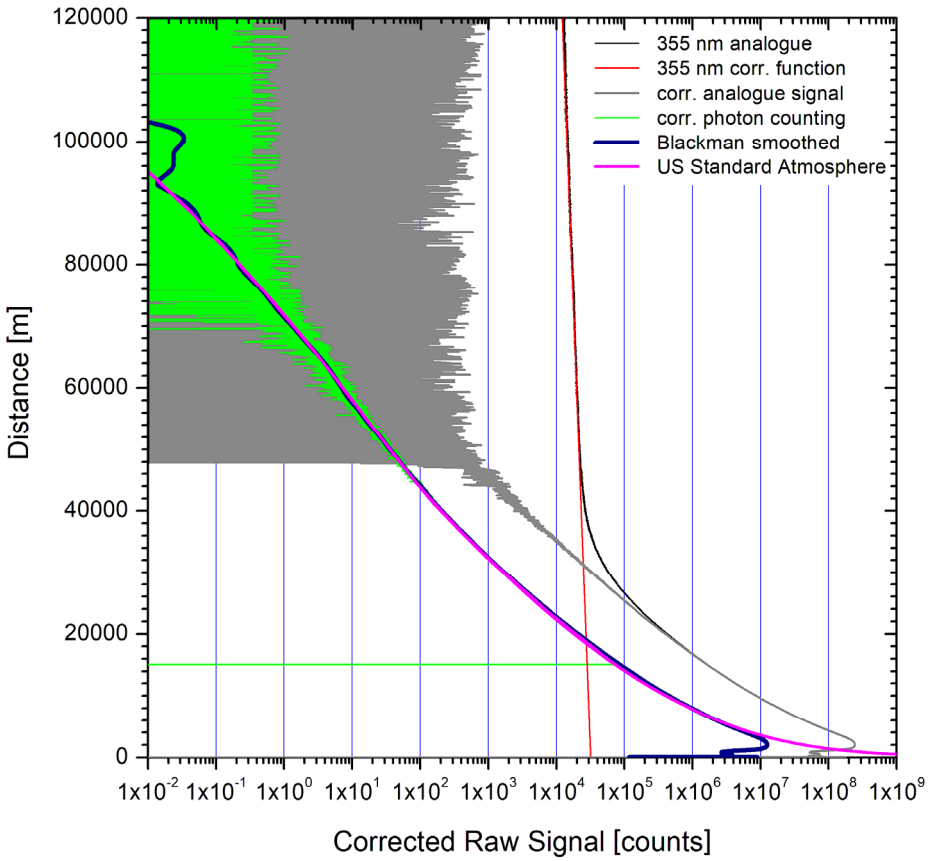

Fig. 1. 355-nm backscatter signals accumulated on 9 October 2021 between 23:05 and 24:01 CET (67171 laser shots) with the transient digitizer (black; corrected: grey) and the photon-counting system (light green); the photon-counting signal starts at 15 km due to a data-acquisition delay (see horizontal green line). Above 100 km just occasionally a single photon was detected (see scale). The combined signal (after calibrating the analogue signal to counts) from both recorders is smoothed with a Blackman-type numerical filter with a range quadratically growing with altitude (blue; see text in Sect. 3.1). For comparison also a synthetic lidar signal simulated with data from the U.S. Standard Atmosphere is shown.

Formatted: Normal, Left, Space After: 500 pt, Line spacing: single

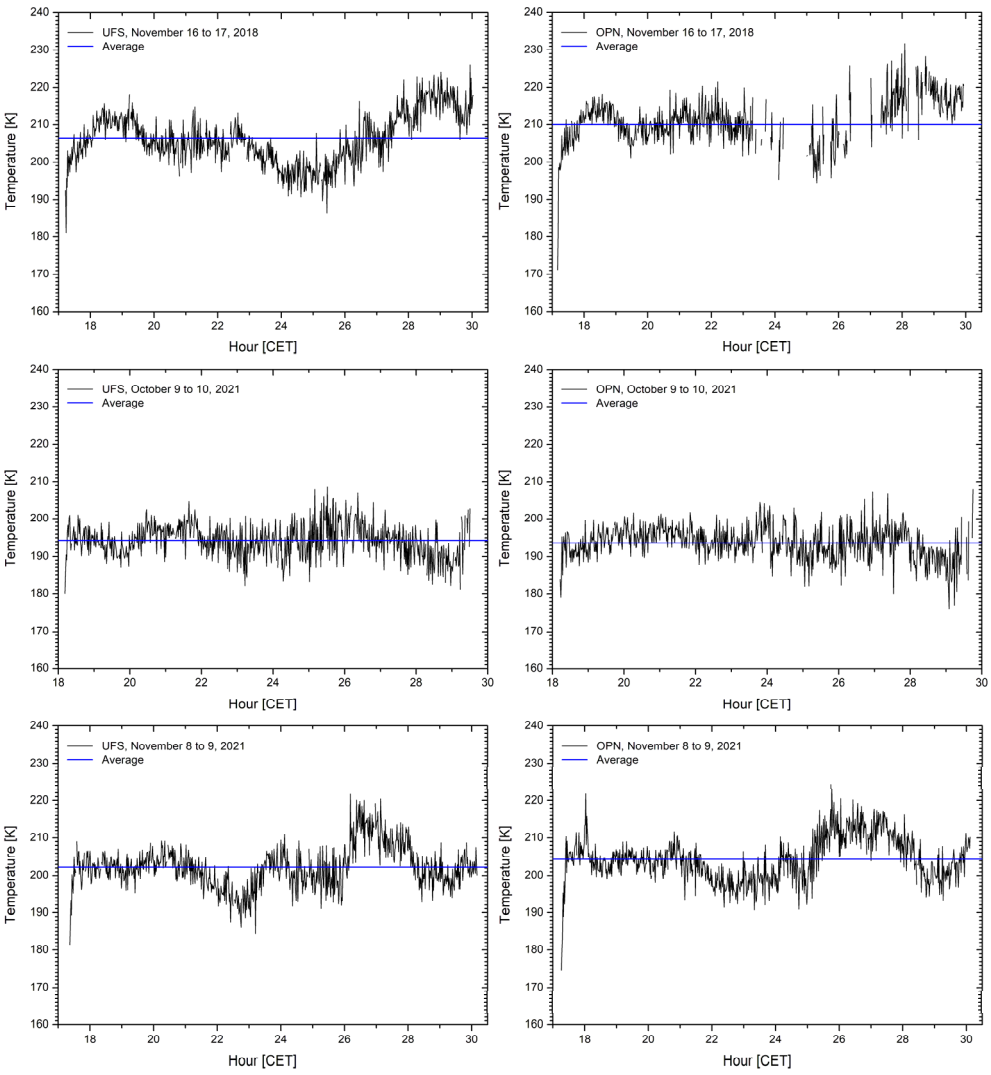

Fig. 2. Examples of GRIPS night-time temperature series at UFS (left column) and Oberpfaffenhofen (OPN, right column) in November 2018, October 2021 and November 2021. There is relatively good agreement for the first two measurements, but in the third case some differences are seen between the results of the two stations. Gaps are due to cloud coverage. The uncertainties at the beginning and the end of a given night is high due to additional daylight.

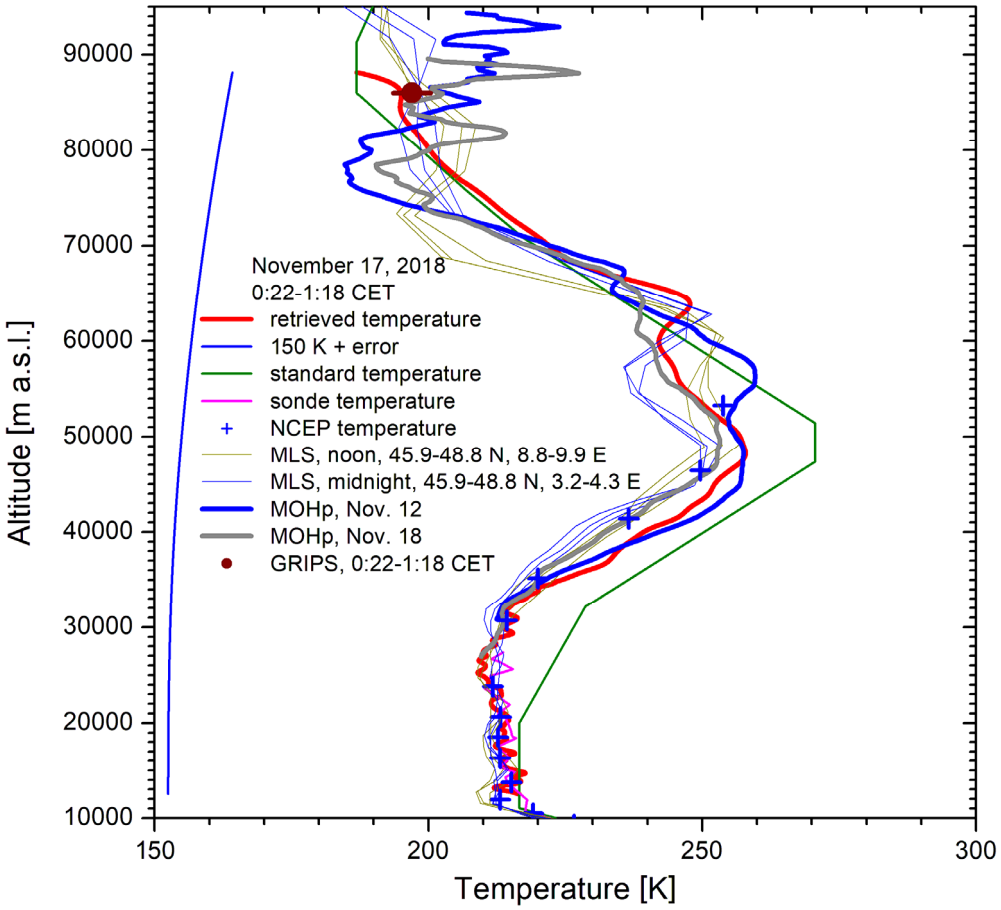

914
915 **Fig. 3.** Temperature measurements on 17 November 2018, compared with data and profiles from other sources
916 (see text).
917
918 **Please, print this figure larger than in single-column format to allow visualizing the details.**
919

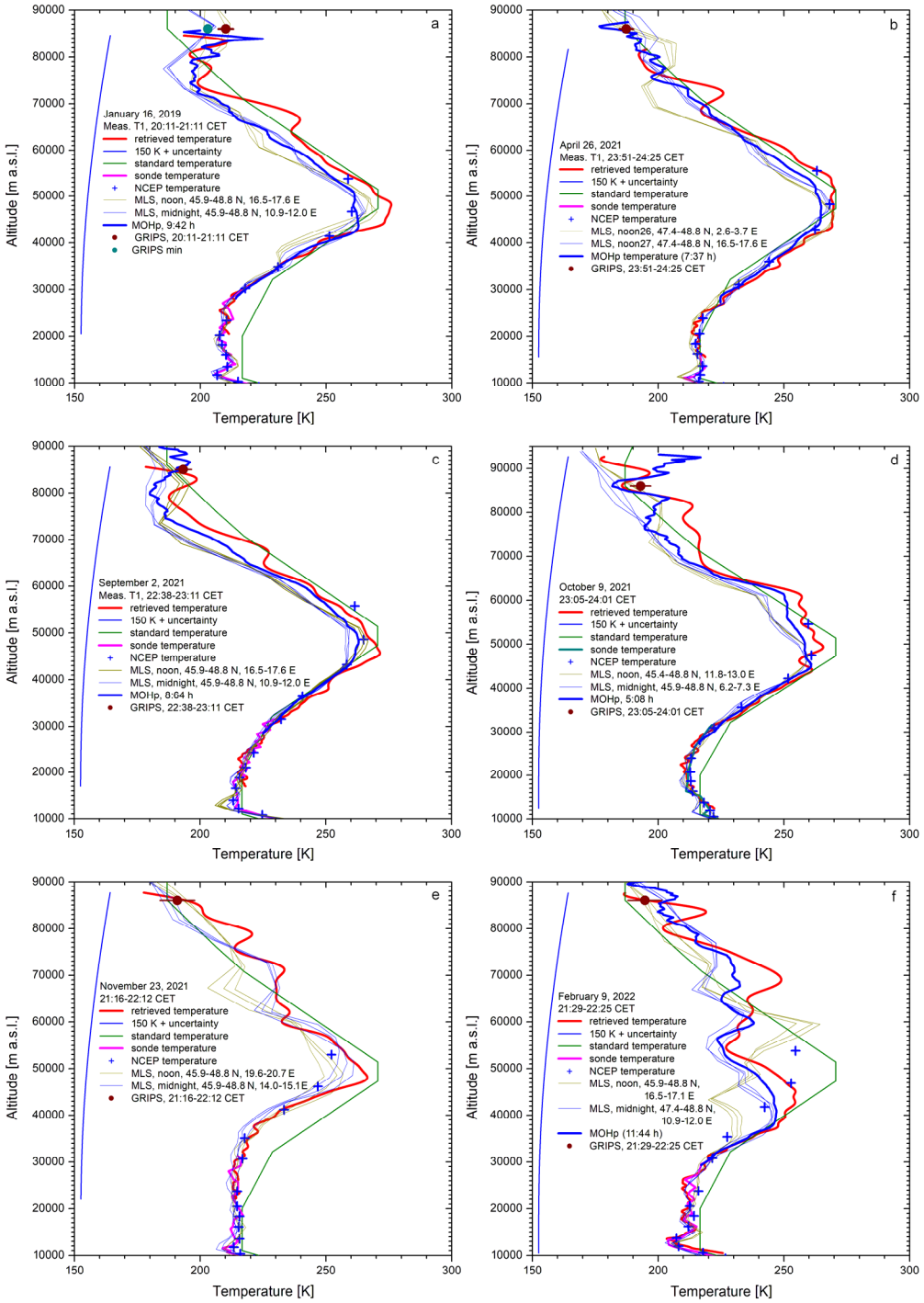

Fig. 4. Six examples of comparisons of temperature profiles from the UFS lidar with the results of other instruments (for details see legends and text). For a given day, we show both the "midnight" and the "noon" MLS profiles. In the case of Panel (b) the "midnight" MLS profiles are missing and those of the neighbouring two "noon" overpasses are displayed.

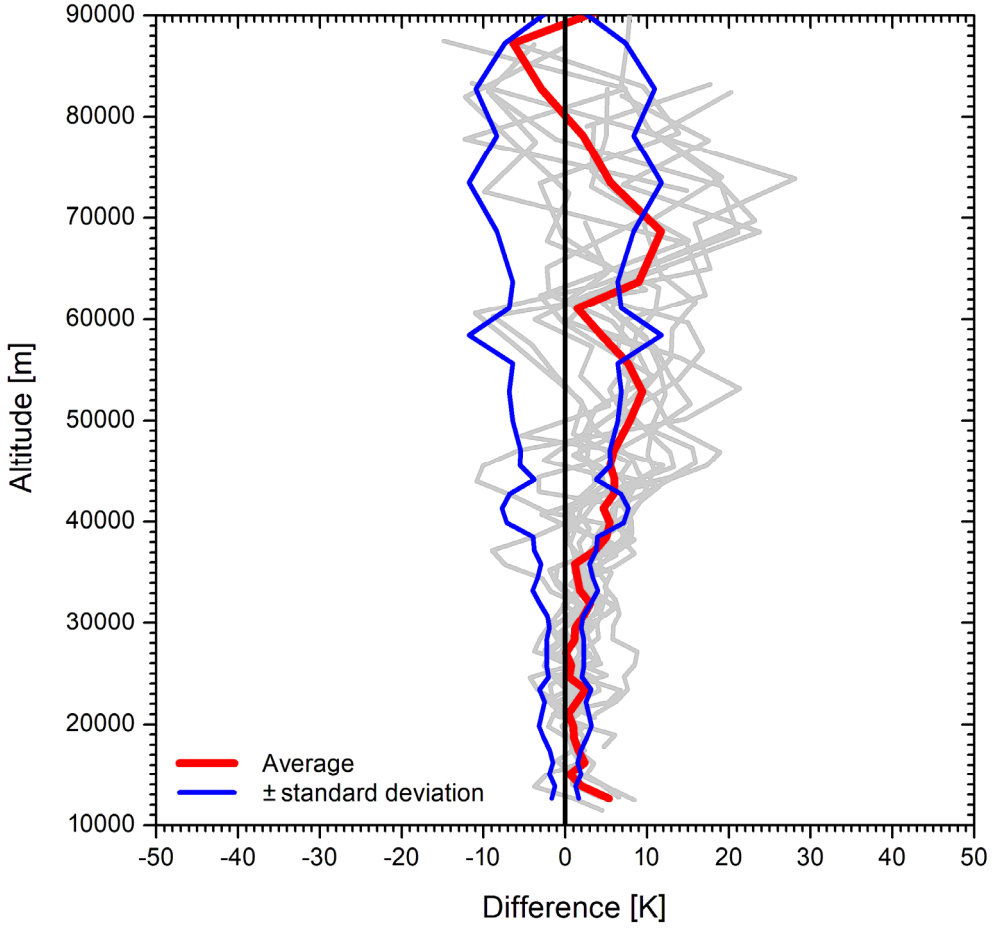

Fig. 5. Differences of the 14 temperature profiles of the UFS lidar and the corresponding measurements of MLS for 47.35° N (grey lines) together with their averages (red line) and standard deviations (blue lines).

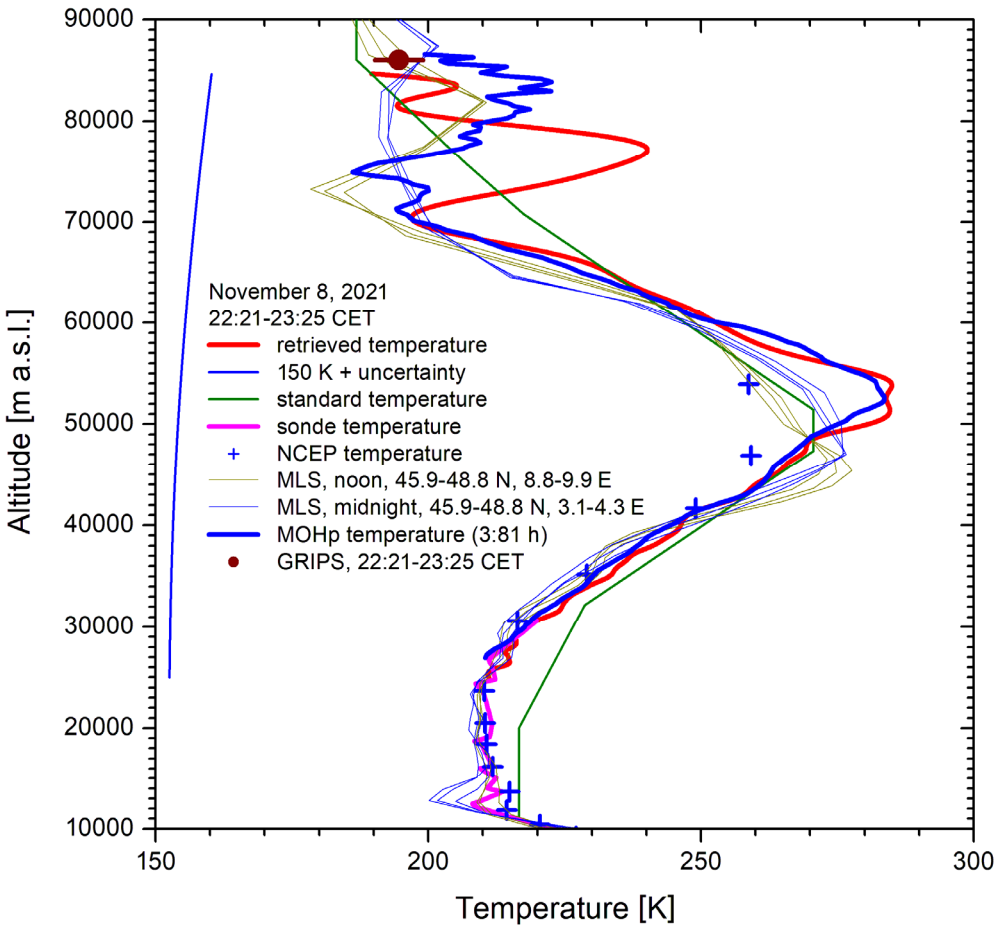

Fig. 6. Comparison of the temperature profile from the UFS lidar on 8 November 2021 with the results of other instruments; here, we observe an almost perfect agreement with the T profile from MOHp up to 70 km, that was taken during a rather short period between 22:30 CET and 1:49 CET, i.e., almost synchronously to the measurement at UFS.

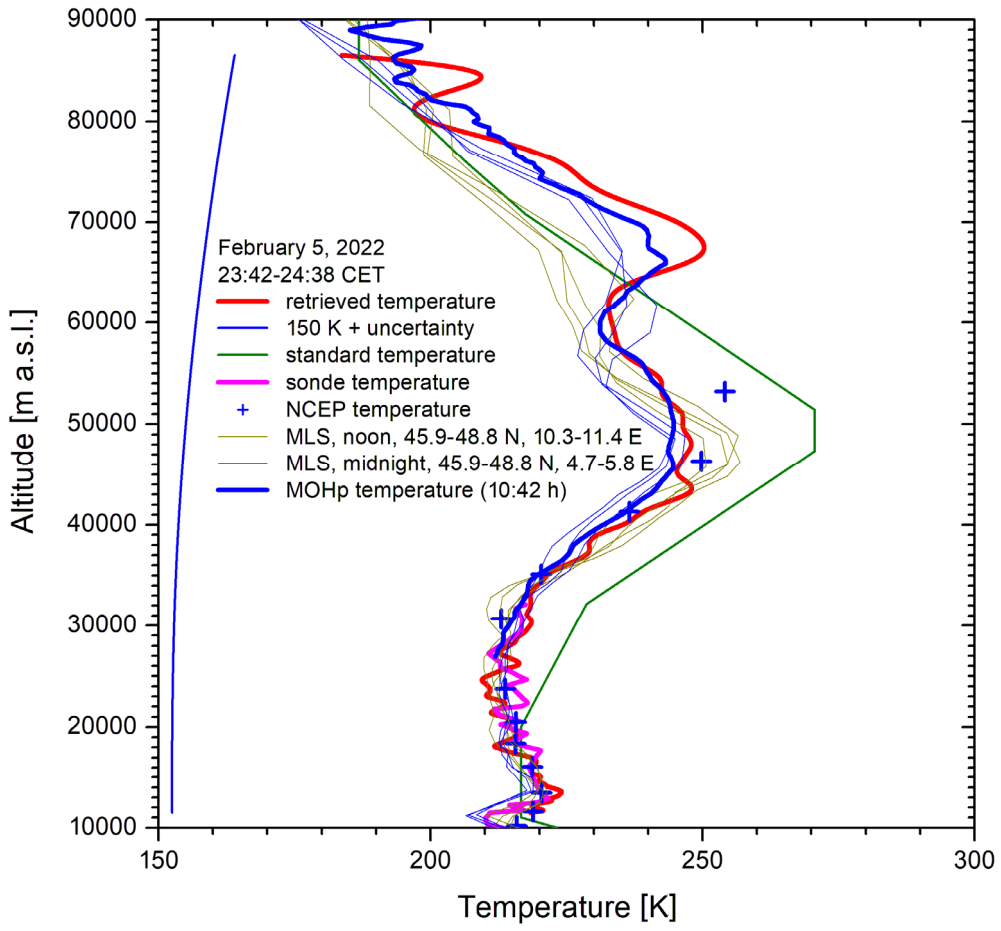

Fig. 7. Comparison of the temperature profile from the UFS lidar on 5 February 2022 with the results of other instruments; here, we observe an almost perfect agreement with the T profile from MOHp, showing rather good agreement up to 65 km. No OH* measurements are available for that night. The reference temperature was chosen to ensure an average temperature matching with ~~the~~ MOHp ~~temperatures~~ above 77 km ~~(disregarding the ringing)~~.

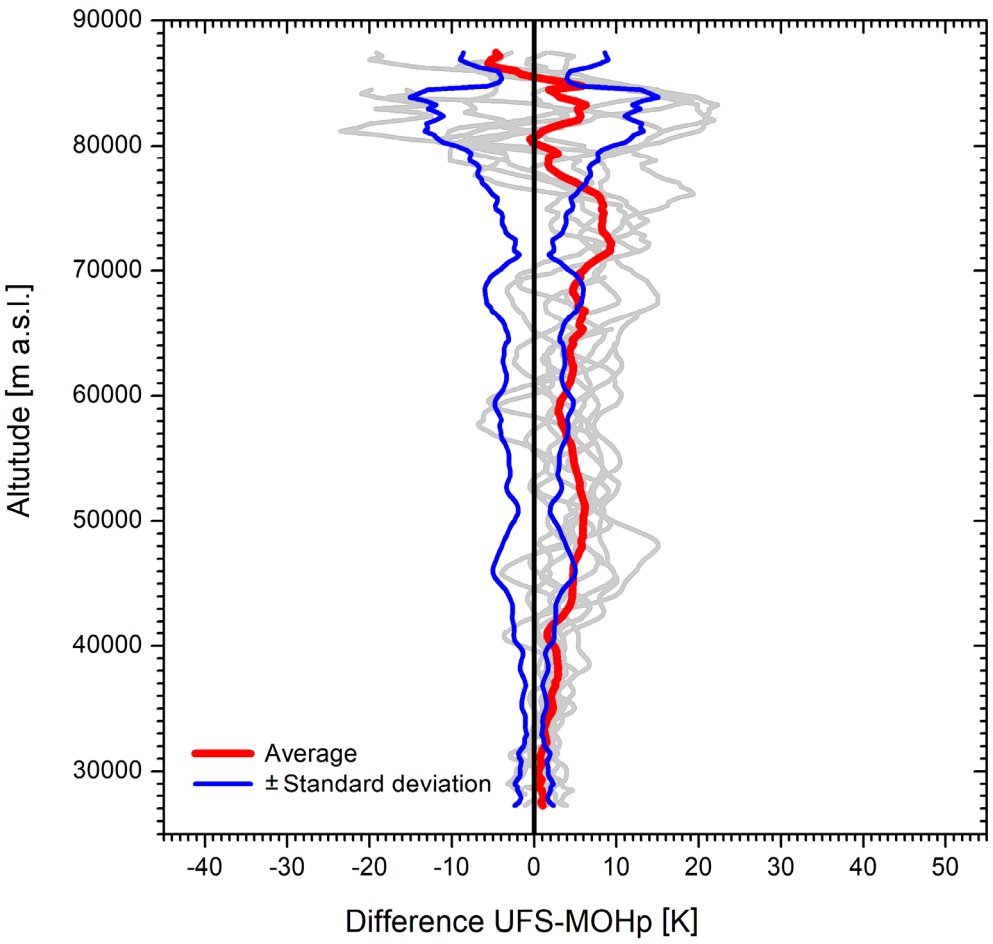

Fig. 8. Differences of the 9 of the 14 temperature profiles of the UFS lidar with those of the MOHp lidar during the same night, together with their averages (red line) and positive and negative standard deviations (blue lines).

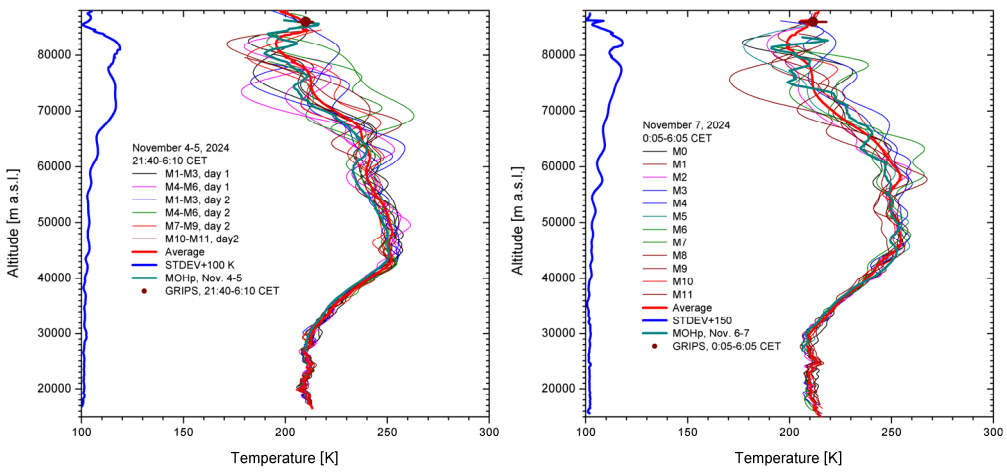

Fig. ~~8~~9. Two of the four night-time series of the UFS 0.5-h temperature profiles in November 2024, compared with the all-night T profiles obtained at MOHp and the GRIPS average during the lidar measurement periods: Left panel: 4 November 2024 (start at 21:40 CET) to 5 November 2014 (end at 6:10 CET, beginning of the dawn); groups of three subsequent profiles (M means measurement) are presented share the same colour in order to reduce confusion.
Right panel: 7 November 2014 (0:05 to 6:05 CET); all profiles for measurements 0 to 11 are coloured differently, from black and violet to red.
The standard deviations (STDEV) are shown in blue after adding 100 K.

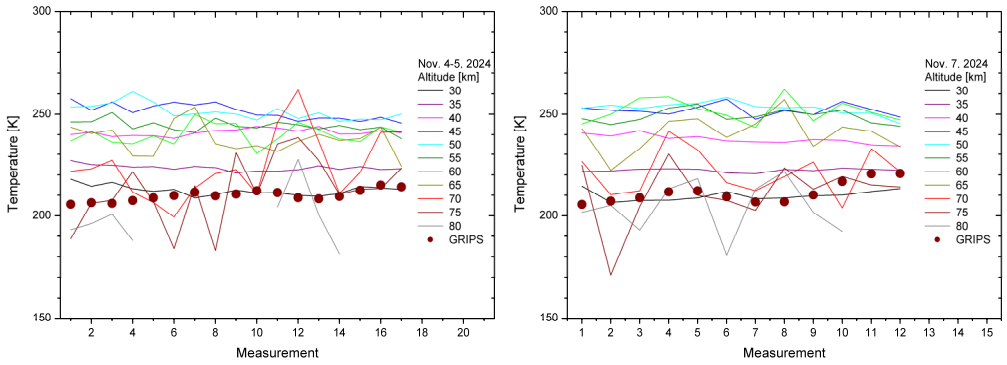

Fig. ~~9~~10. Time series for the two examples shown in Fig. 8 for selected altitudes listed in the legend, together with half-hour averages of the GRIPS temperatures; here, the measurements are labelled from the beginning to the end of the night-time series.

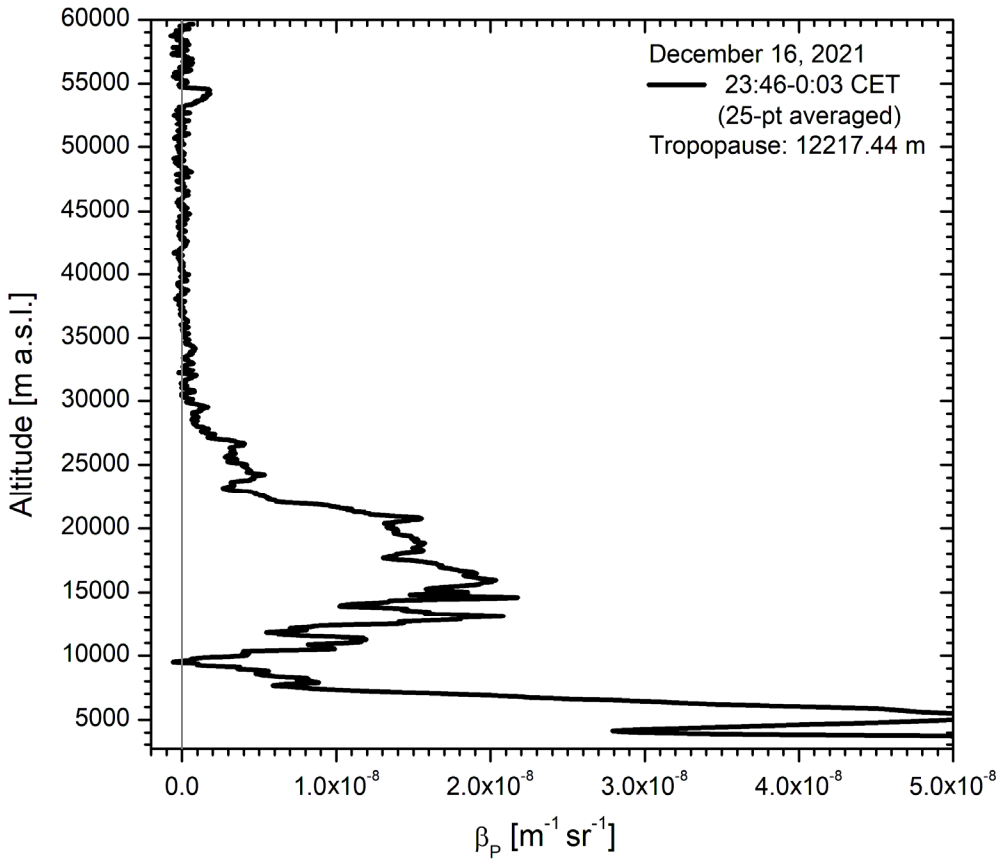

Fig. ~~10~~11. 532.2-nm aerosol backscatter coefficients β_P from a night-time measurement with the UFS stratospheric aerosol lidar showing a strange peak at 54 km.